Low-Speed Stability and Control of Exploratory Tailless Long-Range Supersonic Configurations

Sarah Langston

A thesis
submitted in partial fulfillment of the
requirements for the degree of

Master of Science in Aeronautics and Astronautics

University of Washington

2015

Reading Committee:
Professor Eli Livne, Chair
Affiliate Associate Professor Chester P. Nelson

Program Authorized to Offer Degree:
Aeronautics & Astronautics

University of Washington

Abstract

Low-Speed Stability and Control of Exploratory Tailless Long-Range Supersonic Configurations

Sarah Langston

Chair of the Supervisory Committee:
Professor Eli Livne
Aeronautics and Astronautics

This thesis presents studies of the low-speed stability and control of a representative long-range supersonic flight vehicle. The aircraft of interest is a research uninhabited aerial vehicle (R-UAV), a $1/16^{th}$ scaled model of a concept supersonic business jet. Evaluation of stability and control characteristics is based on a linear time-invariant state-space small-perturbations approach. Low-speed wind tunnel results together with unsteady aerodynamic panel method analysis are the basis for the aerodynamic stability derivatives used. The main goal of this work is to study the effects on stability and controllability of reduction in size or complete elimination of tail surfaces, with particular emphasis on the vertical tail.

TABLE OF CONTENTS

LIST OF FIGURES

LIST OF TABLES

ACKNOWLEDGMENTS

I would like to thank my advisor, Dr. Eli Livne, who gave me the opportunity to learn about aircraft and supersonic flight. He spent many hours supporting me in all aspects of my education, including providing me with academic funding for a full two years. I could never have imagined I could come so far in such a short amount of time under his guidance.

I'd also like to thank the University of Washington, William E. Boeing Department of Aeronautics & Astronautics and the industry representatives who have helped me along the way with various software, including Dr.Marat Mor and Sang Wu. Another thanks to AMA Pilot Chuck Bower for teaching me everything I know about radio controlled airplanes. Additionally, a very special thanks to Chet Nelson whose contribution to my education has been immeasurable.

Most importantly, I'd like to thank my family. They have always believed in me and encouraged me to follow my dreams as an expression of, and guided by, my faith. Their love and support knows no bounds.

DEDICATION

I dedicate this thesis to my parents, Bill and Linda. May I someday have an impact on the world that you both have.

NOMENCLATURE

Acronyms

ARMD	Aeronautics Research Mission Directorate
AFOSR	Air Force Office of Scientific Research
AFRL	Air Force Research Lab
AOA	Angle of Attack
CG	Center of Gravity
CFD	Computational Fluid Dynamics
Coupeville NOLF	Coupeville Naval Outlying Field
EDF	Electric Ducted Fan
ESC	Electronic Speed Controller
ESDU	Engineering Sciences Data Unit
GPS	Global Positioning System
HSCT	High Speed Civil Transport
ICE	Innovative Control Effectors
KWT	Kirsten Wind Tunnel
Lat-Dir	Lateral-Directional
LQR	Linear Quadratic Regulator
LTI	Linear Time Invariant
MAC	Mean Aerodynamic Chord
MPH	Miles per Hour
MDO	Multidisciplinary Design Optimization

NASA	National Aeronautics and Space Administration
N/A	Not Available
ODEs	Ordinary Differential Equations
RFP	Request for Proposal
R-UAV	Research-Uninhabited Aerial Vehicle
RPM	Revolutions per Minute
S&C	Stability and Control
STORM	Supersonic Transport with Optimized Reduced-tail Maneuverability
USAF	United States Air Force
UW	University of Washington

Symbols

$\dot{\alpha}$	Angle of Attack Rate
α	Angle of attack
C_D	Coefficient of Drag
C_L	Coefficient of Lift
ft	Feet
V	Free Stream Velocity
in	Inch
I_x	Moment of Inertia about the x axis
I_{xz}	Moment of Inertia about the xz axis
I_y	Moment of Inertia about the y axis
I_z	Moment of Inertia about the z axis
θ	Pitch Angle
q	Pitch Rate
C_m	Pitching moment coefficient

S	Reference Wing Area
ϕ	Roll Angel
p	Roll Rate
C_l	Rolling moment coefficient
s	Second
C_Y	Side Force Coefficient
β	Sideslip angle
$3D$	Three dimensional
$2D$	Two dimensional
U	Velocity
u	Velocity
c	Wing Chord
b	Wingspan
r	Yaw Rate
C_N	Yawing moment coefficient

Greek Symbols

ζ	Damping ratio
δ	Delta
λ	Eigenvalue
ρ	Freestream air density
ω_n	Natural frequency

Chapter 1
INTRODUCTION

1.1 Background

This thesis presents the creation and testing of a low-speed flight stability and control (S&C) mathematical model of a long range supersonic transport type aircraft for evaluation of the effects of tail surface size reductions. Interest in reducing the size of or completely eliminating tail surfaces is driven by the potential benefits in terms of weight and drag reductions. The development of a research uninhabited aerial vehicle (R-UAV) for reduced-tail or tailless low-speed S&C and handling qualities investigation was presented as a design challenge to seniors at the William E. Boeing Department of Aeronautics and Astronautics at the University of Washington (UW) in the 2014 capstone airplane design course. The capstone airplane design course at the University of Washington in Seattle [1] leads seniors, who begin the course with no prior airplane design experience, through all stages of the airplane design and development process, from conceptual design to the preparation of a prototype for flight, over two academic quarters (20 academic weeks). Significant industry-level analysis and ground testing of components and systems are used, including extensive wind tunnel tests, followed by construction of an all-composites fully instrumented R-UAV for subsequent flight tests.

1.1.1 The University of Washington's 2014 Senior Capstone Airplane Design Project

The potential benefits of the elimination of the vertical tail or its reduction to some minimum size apply to both commercial and military aircraft [2]. Such benefits for any long-range supersonic aircraft include reductions in aircraft weight, skin friction

and form drag, wave drag, and aft-body structural loads. Benefits in radar cross-section may also materialize, leading to improved stealth capabilities for enhanced mission survivability in military applications.

The 2014 capstone airplane design challenge was tackled by a group of thirty-five senior students plus the author of this thesis who served as their teaching assistant. Following the completion of the conceptual design of a full-scale vehicle (to carry two crew members and ten passengers at Mach 1.8 over 4500 miles) the design was geometrically scaled down to a $1/16^{th}$ scale to be built as an R-UAV that would be flight tested to study and validate the low-speed characteristics of the design.

Details of the specific design chosen to meet this challenge can be found in Chapter 3 and in Ref [3]. Like most airplane design challenges, results of this design work can have both civil and military applications.

1.2 Objectives

The main objective of the work described in this thesis is to contribute to the understanding of the consequences of, and technical issues involved with, the elimination of the vertical tail on long-range supersonic configurations, with a focus on the low-speed flight regime.

In particular:

- Creation of state-space linear time-invariant (LTI) mathematical models that would accurately model the stability and control (S&C) characteristics of the designed 2014 UW R-UAV.

- Evaluation of stability and control characteristics at key different flight conditions with different tail sizes.

- Evaluation of stability and control characteristics with basic active flight control with special attention paid to issues of controllability and required level of

activity of control surfaces.

An important note: In a multidisciplinary design optimization (MDO) approach to the design challenge, gains in weight and cost due to the elimination or reduction of tail surfaces might be canceled by weight and costs of active control systems and their hardware if significant control activity and efforts would be required.

1.3 Thesis Structure

A brief survey of past supersonic long-range transports and current concept designs is provided first.

Chapter 3 includes a detailed description of the 2014 UW R-UAV that was built and analyzed. A brief description of the design decision drivers is also presented.

Chapter 4 covers the derivation of the LTI state space model and Chapter 5 explores the creation of the flight dynamic models, including wind tunnel results, of the 2014 UW R-UAV. Chapter 6 presents the inertial properties.

Chapter 7 presents the results of dynamic stability and control analysis of the open-loop R-UAV at three different flight conditions. It also discusses the validity and limitations of the model produced. Chapter 8 studies the close-loop results.

Final conclusions as well as suggestions for future work can be found in Chapter 9.

Chapter 2
LONG-RANGE SUPERSONIC AIRCRAFT

The current chapter includes a brief overview of past and present efforts to design and fly supersonic long-range aircraft.

2.1 Supersonic Transports

A good presentation of the technical challenges that long-range supersonic flight presents can be found in Refs [4] and [5]. The two most widely known commercial supersonic transports are the French-British Concorde and the Russian Tu-144. Neither of these two aircraft survived the challenges imposed by high fuel prices and the tightening of noise and emission level constraints. However, their key design features are worthwhile to note, and they were impressive feats of engineering for their time.

2.1.1 Concorde

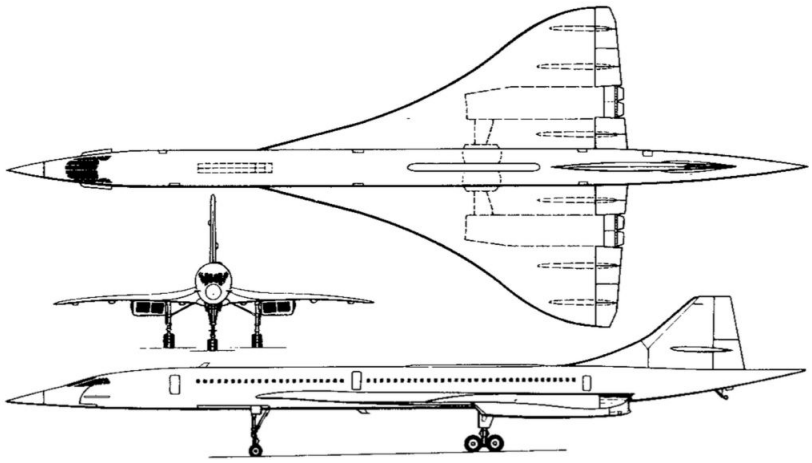

Figure 2.1: 3-View Drawing of Concorde

The main design features of the Concorde (seen in Figure 2.1) from the aerodynamic perspective were its slender fuselage, ogee wing design, variable engine air intake ramp, and a drooped nose section for takeoff and landing. It did not have a canard or an aft horizontal tail and was controlled in pitch by elevons. It did have a large vertical tail. The Concorde's ogee wing design (a kind of a rounded double delta) utilized vortex action for much of its low-speed high-lift. This, coupled with the short moment arm of the trailing edge surfaces to rotate the aircraft, led to high take-off speeds at high angles. This could have possibly been counteracted by the addition of a canard. However, a canard coupled aerodynamically with the wing might have added complexity to the aerodynamic design challenge, including a detrimental impact on lift over drag at high speeds. The support structure necessary for attaching the canard to the front fuselage would have added weight and might have led to a narrowing of the inner fuselage space around the canard area.

2.1.2 Tu-144

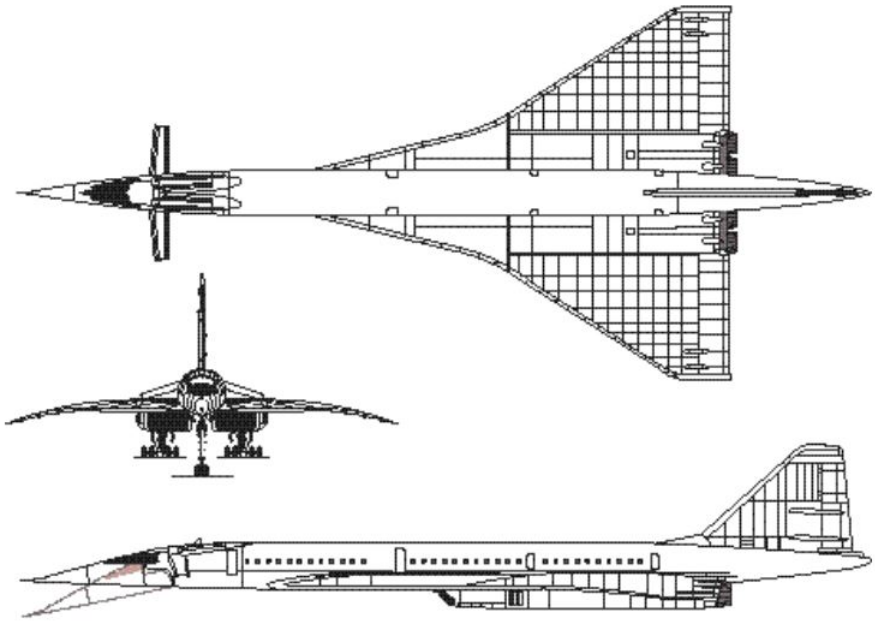

Figure 2.2: 3-View Drawing of Tu-144LL

The Tupolev Tu-144 (as seen in Figure 2.2) was the first supersonic commercial airliner to fly, beating the Concorde to first flight by a few days. The Tu-144 had a very similar design to that of Concorde with a larger double-delta wing that relied on the wings trailing edge surface for longitudinal control. However, the Tu-144 had a canard that provided a nose-up moment for trim. This allowed the elevons to be dropped as flaps, resulting in a higher trimmed coefficient of lift at roughly the same body attitude as the Concorde. This improved take-off and landing performance and significantly improved the handling characteristics during those phases of flight. The canard was then folded back into the body during cruise. In Figure 2.2 one can see the canards and the outline where they fold back into the body. The drooped nose for take-off and landing is also outlined. It should be noted that this is a 3-view drawing of the Tu-144LL, which was a converted Tu-144 used as a flying research laboratory.

The upgrades did not affect the overall aerodynamic shape of the aircraft, and thus the 3-view is representative of the overall Russian design.

2.2 Currently Flying Supersonic Aircraft

The only known supersonic aircraft currently flying are all military aircraft. There have been supersonic bombers and reconnaissance airplanes, but the majority of the aircraft are fighter jets.

The missions of supersonic fighters are very different than those of long-transport aircraft or long-range bombers and lead to very different designs. It would not work aerodynamically to just scale a fighter aircraft up to a commercial transport or any long-range supersonic aircraft size.

2.3 Recent Research for Commercial Supersonic Flight

Research has been going on for years in the United States and around the world into supersonic aircraft design and its aerodynamic, propulsion, structural, stability & control, and environmental impact aspects within the government and industry sectors as well as academia. In addition to the research and development up to the mid 1990s described in Refs [4] and [5], notable efforts include NASAs High Speed Civil Transport (HSCT) effort in the 1990s [6] , [7] , [8] , [9] , [10]. One of NASA's more recent Aeronautics Research Mission Directorate (ARMD) program areas is innovation in commercial supersonic aircraft. NASA had many probes into this area, including the publishing of the N+2 Supersonic Concept Development and Systems Integration report and associated other papers [11] , [12] , [13] , [14], which examines what would be feasible in supersonic technology development in the coming decades.

Within the industry the Aerion Corporation is the only company at this time that has committed to building a supersonic business jet [15]. The Aerion design uses improved laminar flow wings and touts performance characteristics of Mach 1.5 over

oceans with international range. It is not a low sonic boom aircraft, but claims that no boom will reach the ground at Mach 1.2, which would allow the aircraft to fly at supersonic speeds overland in some countries, but not the United States.

Figure 2.3 shows a selection of supersonic long-range aircraft, military and civil, of past years and of more recent not yet materialized conceptual designs. These designs share many common features necessary for efficient supersonic cruise. Some of the features include: high body and nacelle fineness ratios, aft mounted engines, very thin wing and tail airfoils (2-4% max thickness to chord ratio), some variation of a double delta or "cranked" planform, long fore-body ahead of the wing to improve area distribution for minimum wave drag, and relatively large vertical tails to counteract the effect of the large side area ahead of the center of gravity (CG). Figure 2.4 shows a selection of subsonic and trans-sonic tailless flying vehicles, all of them research vehicles. Note the slenderness and low aspect-ratio of the long-range supersonic configurations versus the compact short length of the subsonic tailless vehicles. Such slenderness, with the corresponding length of the fuselage ahead of the wing, leads to stability and control challenges due to the destabilizing effects of the fuselage and vortex shedding by the cross sections of the forward parts of the fuselage. Combined with short spanwise moment arms of wing control surfaces, such configurations, if the vertical tail is removed, present a yaw stability and control challenge.

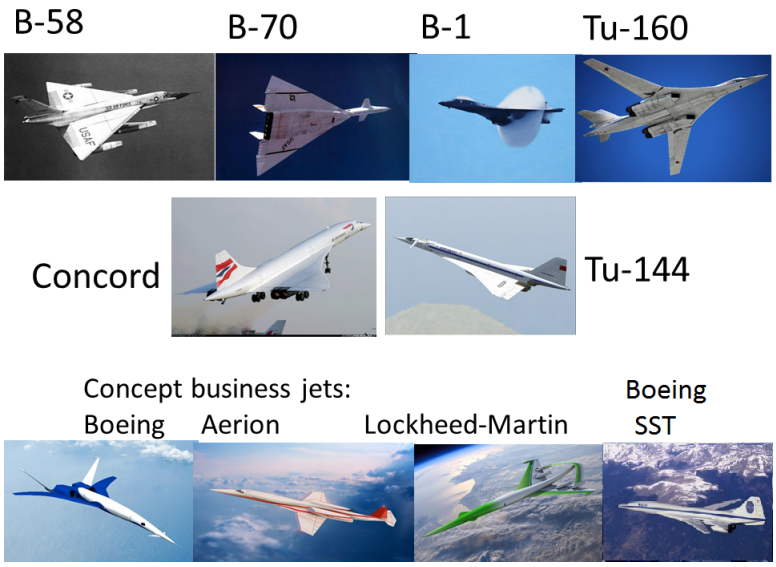

Figure 2.3: Examples of Supersonic Long-Range Configurations

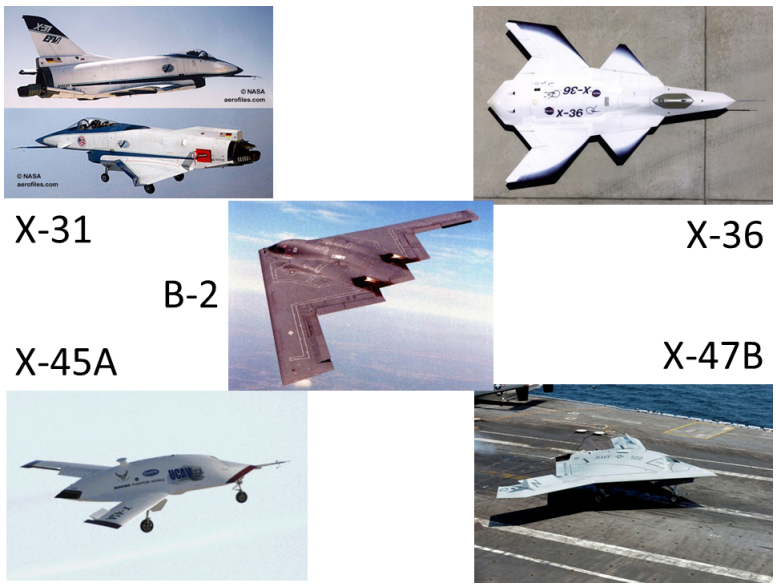

Figure 2.4: Examples of Subsonic Tailless Configurations

Chapter 3

DESIGN AND DESCRIPTION OF 2014 UW R-UAV

The 2014 UW capstone airplane design challenge was to design a long-range supersonic aircraft that would contribute to the understanding of the consequences of eliminating tail surfaces or reducing their size and generate useful computational and experimental data. A detailed report of this endeavor can be found in the class final report, Ref [3]. A full scale airplane was designed first to meet required performance metrics. It was then scaled down geometrically to an R-UAV size in order to study subsonic low-speed characteristics and validate related mathematical models. This chapter describes the design briefly and presents the key properties of the resulting R-UAV.

3.1 Key Design Drivers and Decisions

The full-scale design had to meet the required specifications put forth in a request for proposal (RFP) document. The aircraft had to have a range of 4000nm, flying at Mach 1.6, with two crew members and ten passengers. The resulting design, representative of 100,000 lbs. gross takeoff weight business jet, was scaled down geometrically to drive the R-UAV design. While for stability and control (S&C) research dynamic and not only geometric scaling of the aircraft is required for correct similitude (and that had been the case in some other UW capstone design projects over the years), in 2014 the decision was to pursue geometric scaling only and to focus on the correlation between mathematical models and actual behavior for the R-UAV at hand. Such scaling was considered sufficient for the goal of studying, in an exploratory manner, the aerodynamic controllability and stability of tailless

supersonic configurations at low and high angles of attack.

The R-UAV was allowed some deviations from the full-scale design for simplicity, such as fixed gear and wing leading edges and a simpler engine nacelle design. However, the design in its external and internal features had to remain such that it was still scalable to the business jet size, with provisions for fuel, landing gear storage, and avionics, among other considerations.

3.2 Final Design of R-UAV

The 2014 UW aircraft was code named STORM (Supersonic Transport with Optimized Reduced-tail Maneuverability).

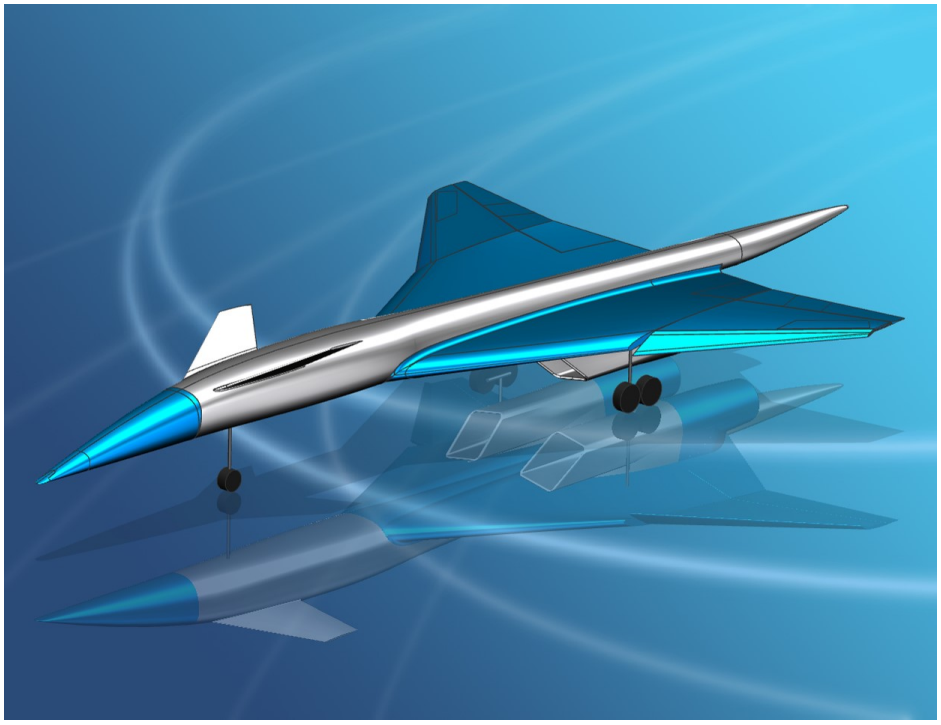

Figure 3.1: Full Scale View of the 2014 UW STORM Aircraft

This full size design was then scaled down to $1/16^{th}$ of the size to create and design the R-UAV. In this thesis from now on all references made to the 2014 UW

aircraft will be in reference to the R-UAV and not the full size aircraft. A 3-view of the R-UAV is presented in Figure 3.2.

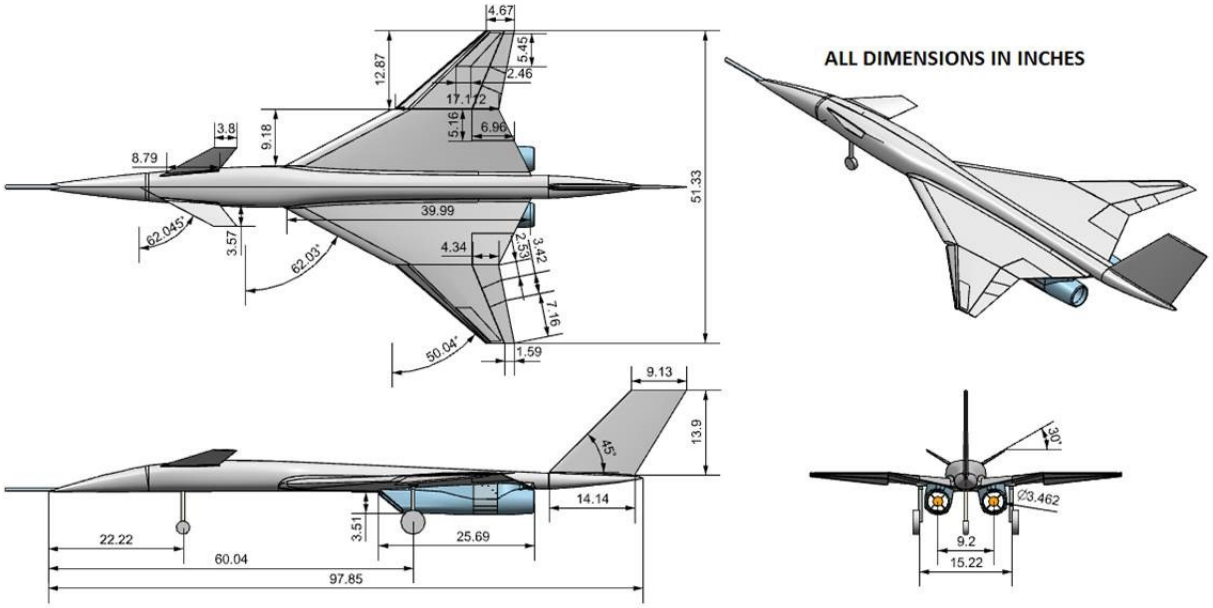

Figure 3.2: 3-View Drawing of the 2014 UW STORM R-UAV

Some key geometric measures of the R-UAV are found in Table 3.1. Both the mean aerodynamic chord (MAC) and wing reference area are computed from an equivalent trapezoidal wing based on the Engineering Sciences Data Unit (ESDU) method.

Table 3.1: Key Geometry Measures of the 2014 UW R-UAV

Aspect Ratio	3
Wingspan	4.3 ft
Length	8.2 ft
Forebody Fineness Ratio	6.52
Mean Aerodynamic Chord (MAC)	25.1 in
MAC distance from center-line	9.56 in
MAC distance ahead of wing crank	6.38 in

3.2.1 Structures

The structural layout of the R-UAV, as a FEMAP generated view of a NASTRAN Finite Element model, is shown in Figure 3.3. The different colors in this figure represent different materials used in the structure. The key materials used are: carbon fiber for the wing skins, fiberglass for the fuselage, a combination of foam-core composite and light plywood for longerons and bulkheads, and fiberglass covered foam for the control surfaces.

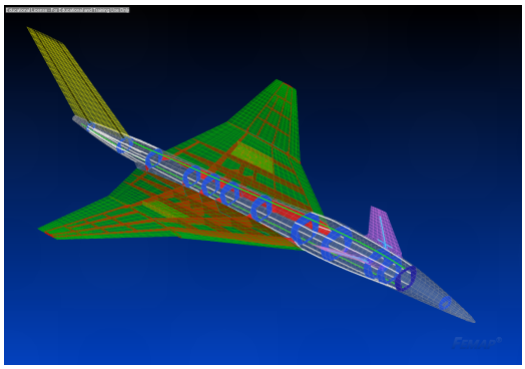

Figure 3.3: FEMAP Model of the Structural Layout of the R-UAV

Two key design drivers for structures, in addition to others, were landing gear positioning and fuel capacity for the full-scale design.

3.2.2 Stability and Control

Handbook equations and figures were used first to obtain approximate configuration characteristics, followed and corrected by CFD analysis using the cd-Adapco STAR-CCM+ un-structured grid Navier-Stokes code. The CFD results were compared to and validated with University of Washington Kirsten Wind Tunnel wind tunnel test data. Details of the wind tunnel testing will be discussed in Section 5.1.

The final control surfaces selected for the UW 2014 R-UAV are shown in Figure 3.4.

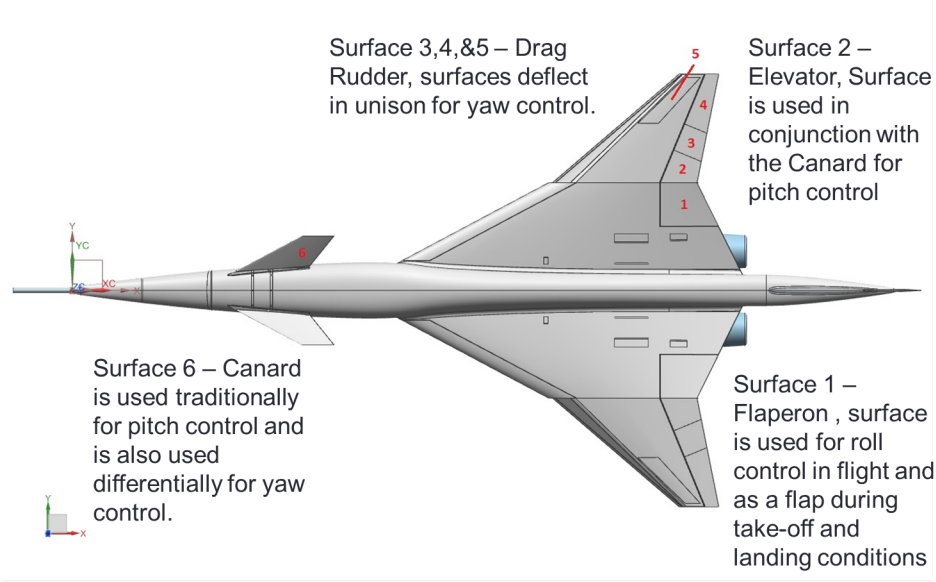

Figure 3.4: STORM Control Surfaces

The airplane has a modular vertical tail that can be replaced by smaller size vertical tails or be removed completely. There is no rudder on the vertical tail. A pair of canards in differential motion, augmented by linked motions of wing spoilers (Surface 5)and drag trailing edge flaps (number 3 & 4 moving one up and one down), provide yaw and roll control. Longitudinal control is provided by the canards moving symmetrically and by elevator control surface 2. Inboard wing flaperons (number 1)provide both roll authority and flap action for take-off and landing. The challenge is to provide adequate control at all flight conditions (limited in the present study to low-speed conditions) together with acceptable stability and handling qualities without active control, if possible, or with active control, if necessary.

CFD

CFD simulations were carried out for both the full-scale and UAV models to guide design decisions. Configuration shape changes studied included wing planform, wing twist, and fuselage blending. Results were validated by the wind tunnel tests at the

University of Washington 12 ft by 8 ft low-speed Kirsten Wind Tunnel.

The CFD analysis was found to be quite accurate overall in the 2014 UW STORM case when compared to the wind tunnel data. That was not the case over the years of designing and testing advanced configurations at the University of Washington, when CFD simulations were found to be sensitive to geometry, mesh, and turbulence models when used to simulate flows over supersonic configurations at high angles of attack and with significant control surface deflections.

Some representative plots of the correlation between CFD predictions and measured wind tunnel results are in Figure 3.5. Note the correct overall trends but shifted curves in the pitching moment versus angle of attack case. Also note the discrepancy between CFD predictions and wind tunnel measurements of the pitching moment curve around an angle of attack of 20 degrees, where a pitch-up tendency predicted by CFD is much more severe than the measured result, illustrating the importance of wind tunnel testing in cases involving high angle of attack and sideslip angles, flow separation, and vortex action and burst.

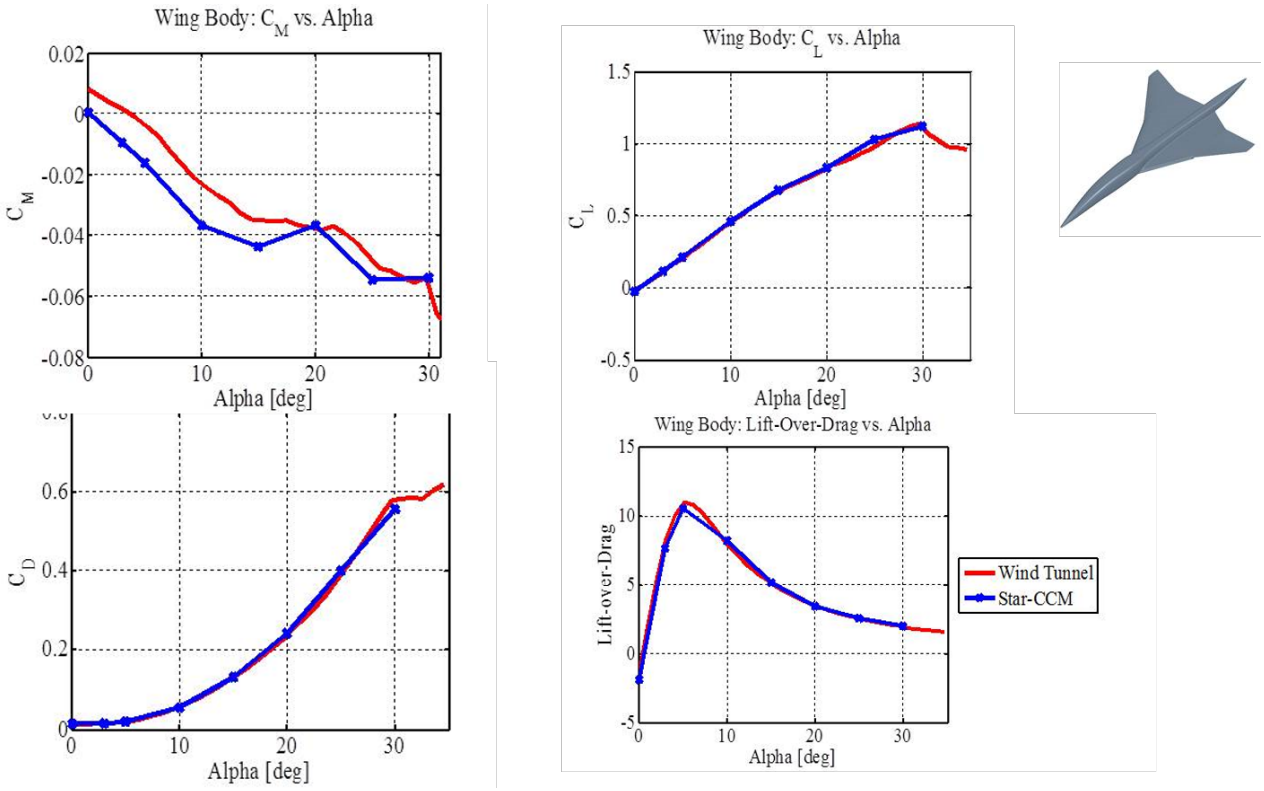

Figure 3.5: CFD and Wind Tunnel Results Comparison

3.2.3 Propulsion

The R-UAV is powered by two 100 mm electric ducted fans (EDFs). These fans produce 11 lbs of static thrust. The EDFs are connected to two electronic speed controllers (ESCs) and powered by four six cell lithium polymer batteries. Each EDF uses two of the batteries connected in series, leading to an approximate flight time of 8 minutes, depending on the mission profile being flown.

3.2.4 Systems and Instrumentation

The R-UAV is outfitted with a data collection system to provide both real time data necessary for safe flight, and also to collect stability and control data that can be used for research purposes.

The R-UAV is equipped with multiple data logging systems, comprised of Eagle Tree and Arduino digital telemetry hardware. The Eagle Tree system allows for real time transmission of data needed for flight, such as airspeed, altitude, RPM, and battery voltage. It also records these values, plus, accelerations and GPS. The Arduino system logs the pilot input signal. Air data systems include alpha/beta vanes and pitot-static nose boom. The R-UAV and its systems are show in Figure 3.6.

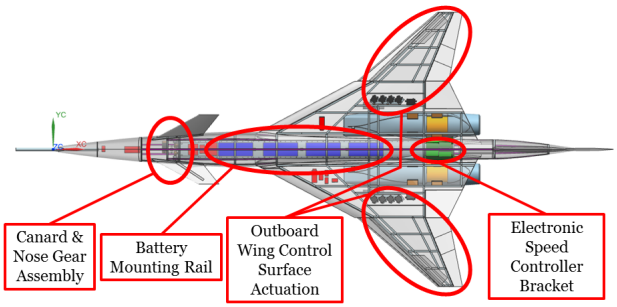

Figure 3.6: Systems Layout of the 2014 UW R-UAV

Control Architecture

In a typical R/C model stability augmentation architecture, six gyros are being used on the prototype R-UAV.

- Gyro 1 is used with the elevators to dampen pitch
- Gyros 2 and 3 drive each canard servo to implement differential canard for yaw damping
- Gyro 4 is used on the nose wheel
- Gyros 5 and 6 - drive each flaperon as an aileron to implement roll damping

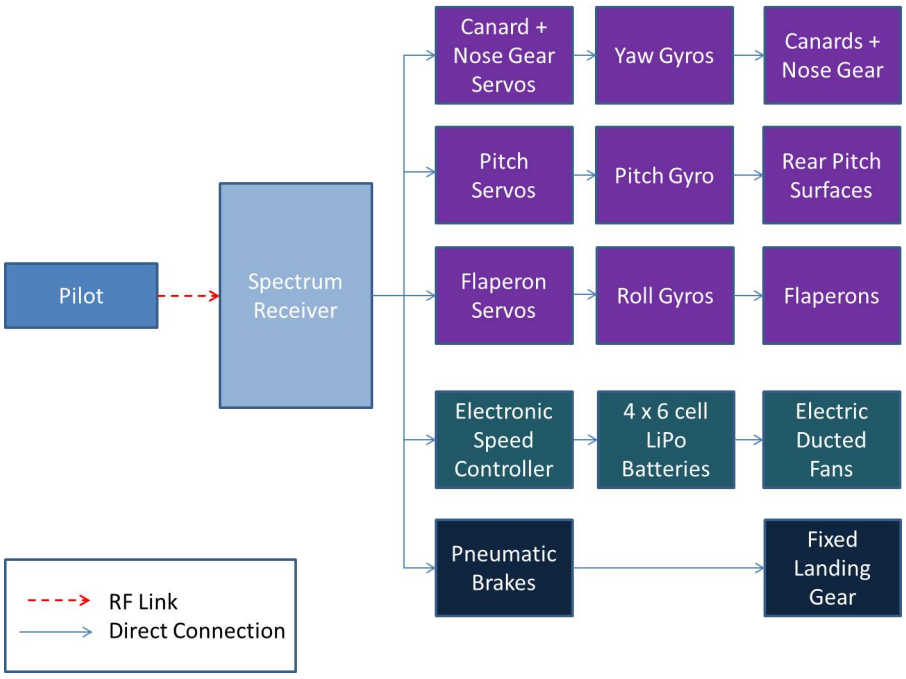

Figure 3.7: First Flight Control Architecture

The control technology exploration approach is conservative and gated in several steps. Changes to the control setup are made incrementally. In preparation for first flights with a full size vertical tail in place, the elevator and canard are mixed 1:1 for pitch control and the differential canard is driven by the gyros only for yaw stability. There is room, however, to implement differential canard into the pilot command for yaw control. All gyros have the ability to be adjusted or turned off during flight if the pilot desires.

Conservatism and safety are emphasized in the planning of first flights of the R-UAV, with full pilot control and rate gyros stability augmentation. The modular design of the UAV allows later reduction in vertical tail size up to elimination of the vertical tail as well as implementation of more advanced active control techniques.

The completed R-UAV is shown in Figures 3.8 and 3.9.

Figure 3.8: Front View of 2014 UW R-UAV with Vertical Tail Removed

Figure 3.9: Top View of 2014 UW R-UAV with Vertical Tail Removed

Chapter 4

LTI LINEAR FLIGHT DYNAMICS STATE SPACE MODEL

Derivation of the small perturbation equations of motion of maneuvering rigid airplanes can be found in many flight stability and control textbooks. The reader is referred to reference [16] for a concise but detailed explanation of the state space models. This chapter includes a brief overview.

Both the longitudinal and lateral-directional dynamics of a rigid aircraft in small perturbation motions can be modeled in the standard state space form of $\{\dot{x}\} = [A]x + \{B\}\delta$, where δ is a scalar input and x is the vector of states . Multiple inputs can be accounted for by using a vector of inputs δ and a corresponding matrix $[B]$. The contributions of aerodynamic, inertial, and flight conditions characteristics to the elements of the [A] and [B] matrices are described in their respective sections below.

4.1 Longitudinal Dynamics

The state space vector describing longitudinal motions consists of:

$$\{x\} = [u/V, \alpha, q, \theta]^T \tag{4.1}$$

Using this state space vector, the coupled set of four first-order ordinary differential equations (ODEs) that describe the linearized airframe longitudinal dynamics become Equation 4.2.

$$[I_n]\{\dot{x}\} = [A_n]\{x\} + \{B_n\}\delta \tag{4.2}$$

Where $[I_n]$ is the inertial matrix:

$$[I_n] = \begin{bmatrix} V & 0 & 0 & 0 \\ 0 & V - Z_{\dot{\alpha}} & 0 & 0 \\ 0 & -M_{\dot{\alpha}} & 0 & 0 \\ 0 & 0 & 0 & 1 \end{bmatrix} \tag{4.3}$$

$$[A_n] = \begin{bmatrix} VX_x & X_\alpha & 0 & -g * cos\theta_0 \\ VZ_u & Z_\alpha & (V + Z_q) & -g * cos\theta_0 \\ VM_u & M_\alpha & M_q & 0 \\ 0 & 0 & 1 & 0 \end{bmatrix} \tag{4.4}$$

And for a single input by an elevator or a canard or a single mix of the two:

$$\{B_n\} = \begin{bmatrix} X_\delta \\ Z_\delta \\ M_\delta \\ 0 \end{bmatrix} \tag{4.5}$$

Because $[I_n]$ is nonsingular, one can premultiply both sides by $[I_n]^{-1}$ and bring the equations to the normal state space form of:

$$\{\dot{x}\} = [A]\{x\} + \{B\}\delta$$

To build the $[A_n]$, $\{B_n\}$ and $[I_n]$ matrices, one needs to find the dimensional stability derivatives from non-dimensional derivatives. Table 4.1 shows the relationship between the two. The non-dimensional derivatives can be obtained by wind tunnel tests, aerodynamic analysis, or system identification during flight tests. All variables in the math models listed here are described in the nomenclature and discussed in [16].

Table 4.1: Longitudinal Dimensional Stability Derivatives

Term	Description	Units
X_u	$-\frac{QS}{mV}(2C_D + M\frac{\partial C_D}{\partial M})$	s^{-1}
X_α	$-\frac{QS}{m}(C_L - \frac{\partial C_D}{\partial \alpha})$	$ft * s^{-2}$
$X_{\dot{\alpha}}$	$-\frac{QS}{m}(\frac{c}{2V}(\frac{\partial C_D}{\partial \frac{\dot{\alpha}c}{2V}})$	$ft * s^{-1}$
X_q	$-\frac{QS}{m}(\frac{c}{2V}(\frac{\partial C_D}{\partial \frac{qc}{2V}})$	$ft * s^{-1}$
X_δ	$-\frac{QS}{m}(\frac{\partial C_D}{\partial \delta})$	$ft * s^{-2}$
Z_u	$-\frac{QS}{mV}(2C_L + M\frac{\partial C_L}{\partial M})$	s^{-1}
Z_α	$-\frac{QS}{m}(C_D - \frac{\partial C_L}{\partial \alpha})$	$ft * s^{-2}$
$Z_{\dot{\alpha}}$	$-\frac{QS}{m}(\frac{c}{2V}(\frac{\partial C_L}{\partial \frac{\dot{\alpha}c}{2V}})$	$ft * s^{-1}$
Z_q	$-\frac{QS}{m}(\frac{c}{2V}(\frac{\partial C_L}{\partial \frac{qc}{2V}})$	$ft * s^{-1}$
Z_δ	$-\frac{QS}{m}(\frac{\partial C_L}{\partial \delta})$	$ft * s^{-2}$
M_u	$-\frac{QSc}{I_y V}M\frac{\partial C_m}{\partial M}$	$ft^{-1} * s^{-1}$
M_α	$-\frac{QSc}{I_y}(\frac{\partial C_m}{\partial \alpha})$	s^{-2}
$M_{\dot{\alpha}}$	$-\frac{QSc}{I_y}(\frac{c}{2V}(\frac{\partial C_m}{\partial \frac{\dot{\alpha}c}{2V}})$	s^{-1}
M_q	$-\frac{QSc}{I_y}(\frac{c}{2V}(\frac{\partial C_m}{\partial \frac{qc}{2V}})$	s^{-1}
M_δ	$-\frac{QSc}{I_y}(\frac{\partial C_m}{\partial \delta})$	s^{-2}

4.2 Lateral-Directional Dynamics

The lateral-directional equations are also derived in [16]. The lateral-directional state space vector consists of:

$$\{x\} = [\beta, p, \phi, r]^T \tag{4.6}$$

Using this state space vector, the coupled set of four first-order ordinary differential equations (ODEs) that describe the linearized airframe lateral-directional dynamics become, for the single input, Equation 4.7.

$$[I_n]\{\dot{x}\} = [A_n]\{x\} + \{B_n\}\delta \tag{4.7}$$

Where $[I_n]$ is the inertial matrix for lateral-directional small perturbation motion:

$$[I_n] = \begin{bmatrix} V & 0 & 0 & 0 \\ 0 & 1 & 0 & -\frac{I_{xz}}{I_x} \\ 0 & 0 & 1 & 0 \\ 0 & -\frac{I_{xz}}{I_z} & 0 & 1 \end{bmatrix} \tag{4.8}$$

And

$$[A_n] = \begin{bmatrix} Y_\beta & Y_p & g * cos\theta_0 & Y_r - V \\ L_\beta & L_p & 0 & L_r \\ 0 & 1 & 0 & 0 \\ N_\beta & N_p & 0 & N_r \end{bmatrix} \tag{4.9}$$

$$\{B_n\} = \begin{bmatrix} Y_\delta \\ L_\delta \\ 0 \\ N_\delta \end{bmatrix} \tag{4.10}$$

Because $[I_n]$ is nonsingular, both sides of the equation can be multiplied by $[I_n]^{-1}$ and the equations are brought to the standard state space form of:

$$\{\dot{x}\} = [A]\{x\} + \{B\}\delta$$

To build the $[A_n]$, $\{B_n\}$ and $[I_n]$ matrices, non-dimensional stability derivatives, inertial properties, and flight conditions are used to create the dimensional derivatives. Table 4.2 shows the equations for the lateral-directional dimensional derivatives.

Table 4.2: Lateral-Directional Dimensional Stability Derivatives

Term	Description	Units
Y_β	$\frac{QS}{m}(\frac{\partial C_y}{\partial \beta})$	$ft * s^{-2}$
Y_p	$\frac{QS}{m}(\frac{b}{2V}(\frac{\partial C_y}{\partial \frac{pb}{2V}})$	$ft * s^{-1}$
Y_r	$\frac{QS}{m}(\frac{b}{2V}(\frac{\partial C_y}{\partial \frac{rb}{2V}})$	$ft * s^{-1}$
Y_δ	$\frac{QS}{m}(\frac{\partial C_y}{\partial \delta})$	$ft * s^{-2}$
L_β	$\frac{QSb}{I_x}(\frac{\partial C_l}{\partial \beta})$	s^{-2}
L_p	$\frac{QSb}{I_x}(\frac{b}{2V}(\frac{\partial C_l}{\partial \frac{pb}{2V}})$	s^{-1}
L_r	$\frac{QSb}{I_x}(\frac{b}{2V}(\frac{\partial C_l}{\partial \frac{rb}{2V}})$	s^{-1}
L_δ	$\frac{QSb}{I_x}(\frac{\partial C_l}{\partial \delta})$	s^{-2}
N_β	$\frac{QSb}{I_z}(\frac{\partial C_n}{\partial \beta})$	s^{-2}
N_p	$\frac{QSb}{I_z}(\frac{b}{2V}(\frac{\partial C_n}{\partial \frac{pb}{2V}})$	s^{-1}
N_r	$\frac{QSb}{I_z}(\frac{b}{2V}(\frac{\partial C_n}{\partial \frac{rb}{2V}})$	s^{-1}
N_δ	$\frac{QSb}{I_z}(\frac{\partial C_n}{\partial \delta})$	s^{-2}

By adding an observation (output) equation to the linearized state space equations above, a set of equations is obtained linking inputs to outputs, allowing for the implementation of active control by linking inputs to state behavior or to output behavior:

$$\{\dot{x}\} = [A]\{x\} + [B]\{\delta\} \tag{4.11}$$

$$\{y\} = [C]\{x\} + [D]\{u\} \tag{4.12}$$

The matrix [C] determines the effects of the states on the output. The matrix [D] provides a channel for direct influence of the inputs on the outputs when such direct input-output influence is present in the modeled system.

Chapter 5

CREATION OF THE R-UAV STATE SPACE FLIGHT DYAMIC MODELS

The creation of the mathematical dynamic and control model for the 2014 UW R-UAV is described in this chapter. While CFD results for the static aerodynamic derivatives were available initially, they were replaced by the derivatives based on the results of the Kirsten Wind Tunnel tests. For dynamic stability derivatives (aerodynamic derivatives modeling the effects of rotation rates) an unsteady aerodynamic code had to be used [17] [18].

Both NASTRAN in its aeroelastic analysis capacity and Zona Technology's ZAERO can produce stability derivatives based on linear unsteady aerodynamics, with ZAERO including a more advanced modeling of 3D bodies and body / lifting-surface coupling than NASTRAN. The NASTRAN unsteady aerodynamic modeling is based on the Doublet Lattice Method coupled, for the body effects, with slender body theory. The ZAERO aerodynamic theory is described by Refs [19] and [20]. The ZAERO model of the 2014 UW R-UAV was used in this work to obtain stability derivatives for the configuration.

5.1 Wind Tunnel

The wind tunnel model of the 2014 UW R-UAV underwent two separate entries of wind tunnel testing at the Kirsten Wind Tunnel (KWT). This is a subsonic wind tunnel located at the University of Washington in Seattle as part of the University of Washington Aeronautical Laboratory. The first tests took place in April 2014 as part of the 2014 senior design class and project. During that test, lasting 8 days, the

final configuration of the aircraft was finalized and preliminary control surface data was found. The second, shorter, KWT test entry took place in January 2015 and was focused on further exploring the control surface effectiveness.

5.1.1 Set-up

The 2014 STORM wind tunnel model is a 1:1 scale model of the R-UAV manufactured by AeroTEC, a company in Seattle, to students' specifications. The model was machined primarily out of aluminum, wood, and high-density foam. The control surfaces used for deflections were either 3D printed or manufactured by students during the tests out of sheet metal to quickly study different control surface configurations and sizes.

The first stages of testing focused on finding an initial configuration that would lead to a statically stable aircraft for first flight. Figure 5.1 shows the final configuration chosen for the R-UAV. This configuration includes an oversized vertical tail to ensure lateral-directional stability during first flights.

Figure 5.1: Final Configuration for R-UAV First Flight

The model was tested in many different configurations. Figure 5.2 show the model

without the vertical tail - the ultimate interest of the project.

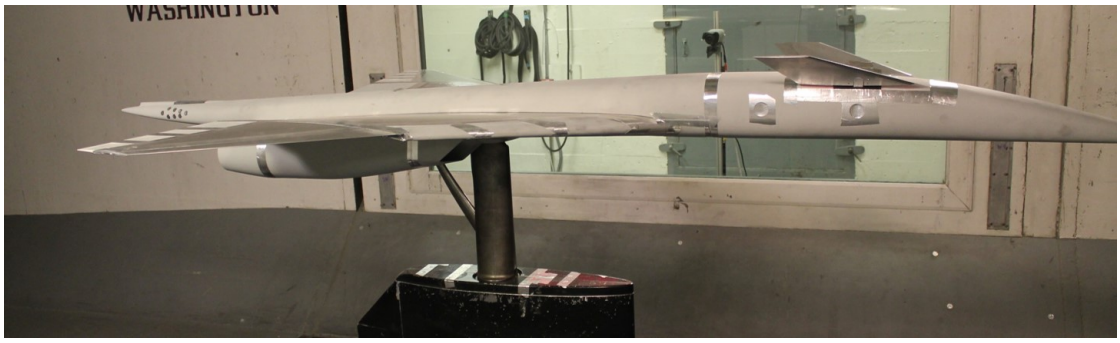

Figure 5.2: Wind Tunnel Model with No Vertical Tail

In addition to the characterization of the R-UAV final configuration and determining the control surface deflections required, a low-boom nose was also tested to study the effects of the longer nose representative of low sonic-boom designs, on yaw stability. The low boom nose can be seen in figure 5.3. This nose was an 11:1 length to diameter ratio. This is considered within the expected threshold of fineness that would lead to acceptable levels of sonic boom intensity for future overland supersonic flight.

Figure 5.3: Wind Tunnel Model with Low Boom Nose Installed

Results from the wind tunnel tests for the variation of forces and moments as functions of angle of attack, side-slip angle, and control surface deflections were corrected to account for tunnel wall effects. The data was then used to obtain stability derivatives with respect to three flight conditions / configuration combinations by linearization. The conditions of interest are: Low angle of attack and high angle of attack in the cruise configuration as well as a high angle of attack condition for the configuration with flaps at 15 degrees, representing a take-off and landing condition.

5.2 Static Stability Derivatives

The final configuration of the aircraft with the full-size vertical tail and conventional forward fuselage was found to be statically stable in all axes: a negative pitching moment coefficient versus lift coefficient slope, a positive yawing moment coefficient versus side-slip angle slope, and a stable dihedral effect for roll stability.

Testing in the wind tunnel made it possible to find static stability derivatives across a wide range of angles of attack. The derivatives at the three different flight conditions of interest are shown in Table 5.1.

It was found that both the longitudinal and lateral-directional derivatives were very linear between 0 and 8 degrees angle of attack. The lateral-directional coefficients began to exhibit nonlinearities around 15 degrees angle of attack, and the configuration encountered pitch-up around 28 degrees angle of attack. Due to this, the aircraft is limited to flight below 26 degrees angle of attack.

Table 5.1: R-UAV Static Stability Derivatives at Three Different Flight Conditions (per radian)

Derivative Per Radian	Low α High Speed Cruise	High α Low Speed	High α Flaps 15° Low Speed Take-off/Landing
CD_0	0.030514	0.17086057	0.1721
CD_α	0.04411775	1.149353337	1.2345
CL_0	0.076486	0.7598692	0.8317
CL_α	2.97766	2.70779854	2.7052
CM_0	0.051367	-0.00705205	-0.0526
CM_α	-0.274446784	-0.133499166	-0.1053
CY_β	-0.62681583	-0.241982359	-0.263812051
Cl_β	-0.11015114	-0.206389584	-0.19992662
CN_β	0.14089425	0.064311	0.067244

Control surface derivatives at the three flight conditions of interest are listed in Table 5.2.

Table 5.2: R-UAV Control Surface Derivatives at Three Different Flight Conditions (per degree of surface deflection)

Derivative	Low α High Speed Cruise	High α Low Speed	High α Flaps 15° Low Speed Take-off/Landing
$CD_{\delta Elevator}$	0.027261332	-0.0429529	-0.041915724
$CD_{\delta Canard}$	0.04941188	0.0769445	0.077732038
$CL_{\delta Elevator}$	-0.481341844	-0.23706835	-0.251092949
$CL_{\delta Canard}$	0.066394349	0.00125253	0.008882558
$CM_{\delta Elevator}$	0.231050961	0.11055902	0.116986965
$CM_{\delta Canard}$	0.1597922	0.05943207	0.072419297
$CY_{\delta DragRudder}$	-0.02391064	-0.016486613	-0.016708157
$CY_{\delta Flaperon}$	0.016760257	0.024010454	0.020460408
$CY_{\delta DifferentialCanard}$	0.0924467	0.194918841	0.185520042
$Cl_{\delta DragRudder}$	0.0121496	0.007075901	0.006924641
$Cl_{\delta Flaperon}$	0.05011595	0.051721494	0.052117981
$Cl_{\delta DifferentialCanard}$	-0.009511	0.00747137	0.006853
$CN_{\delta DragRudder}$	0.020264021	0.013143284	0.013118838
$CN_{\delta Flaperon}$	0.015705537	-0.017367709	-0.015990318
$CN_{\delta DifferentialCanard}$	0.07769	0.111531901	0.111301572

5.3 Forward Fuselage Effects

Slender supersonic configurations at high angles of attack are notorious for the effects of the cross sectional shape of the forward fuselage on the vortices shed left or right and the resulting effect on lateral directional stability. Comparing the yawing moment coefficient as a function of angle of attack at zero side-slip angles shown in Figure 5.4, the nonlinearity of the behavior is obvious. The tendency to throw the nose to the left or right when angles of attack are increased is commonly termed yaw-slice or nose-slice.

This tendency was corrected with body length chines on the final R-UAV configuration, which can be seen in Figures 3.8 and 3.9.

It is worth noting that the yaw slice phenomenon is not too severe on the low-boom nose, as the instability does revert back towards zero yawing moment rather

than continuing one direction. It could most likely be corrected with implementation of longer chines and a yaw damping system on a full scale aircraft.

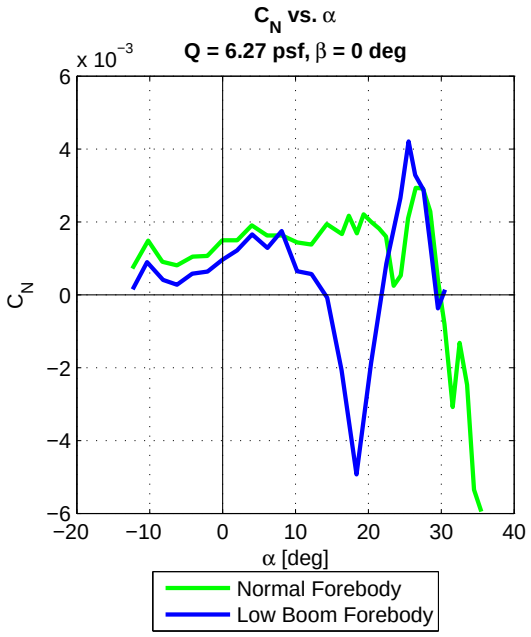

Figure 5.4: Yaw Slice Behavior Comparison between Final Configuration and Low Boom Nose Configuration

5.4 Wind Tunnel Results - Static Stability

The final configuration was shaped to give the R-UAV static stability with a flight center of gravity at 15% of the mean aerodynamic chord (MAC).

The lift curve slope (see Figure 5.5) shows that this configuration has a negative C_L at 0 angle of attack which leads to flight at a higher body alpha. This is potentially detrimental to the subsonic S&C, and is due to the forebody area above the plane of the wing disappearing into the wing as one moves aft. This, however, is good for supersonic cruise, providing greater potential cruise lift over drag.

The pitching moment versus angle of attack curve (see Figure 5.6) shows a statically stable airplane with no pitch up up to near 30° angle of attack. Note that as

the angle of attack is increased on this configuration the two unstable pitch/angle of attack regions around 19-22 and 26-30 degrees are followed by stable regions. Nevertheless the R-UAV was deemed flyable with an alpha limit of 26 degrees to avoid any encounter with significant pitch up.

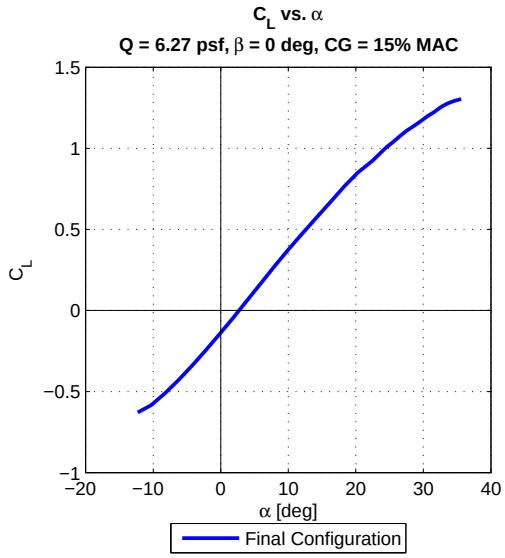

Figure 5.5: Lift Curve for the Final Configuration of the 2014 R-UAV

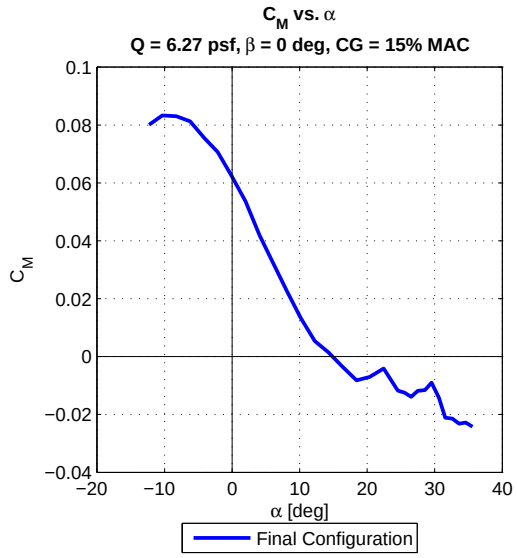

Figure 5.6: Pitching Moment for the Final Configuration of the 2014 R-UAV

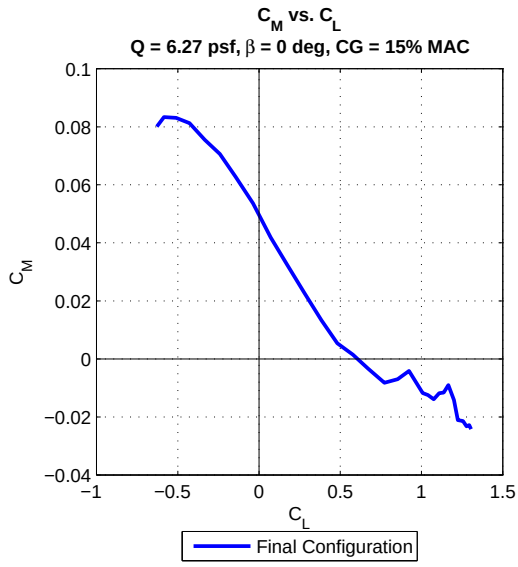

Figure 5.7: C_m verses C_L for the Final Configuration of the 2014 R-UAV

Regarding stability in yaw of the final configuration with the large vertical tail, It

can be seen in Figure 5.8 that the yawing stability deteriorates as the angle of attack increases beyond 8 degrees.

For $0°\beta$ yaw instability emerges as the angle of attack approaches and exceeds $15°\alpha$. However, once the side-slip angle becomes larger than 5 degrees (approximately) directional stability is regained all the way to an angle of attack of 24 degrees.

The localized instability around zero β is not of concern from a static stability perspective provided the largest deviation occurs at angles of attack beyond the normal operating range and adequate yaw control is available to keep the aircraft aligned. This could be done with either pilot intervention or yaw augmentation.

The over-sized vertical tail used conservatively for first flight has excessive "weather-cock" or yaw stability, and reducing the tail to an intermediate size would be beneficial. This will be done as soon as the novel yaw control devices can be proven effective in flight.

One possibility considered was that at high angles of attack the tail, now lower with respect to the strut and pylon in the test section that support the model, may be affected by the flow around the wind tunnel strut / pylon support and thus lose stabilizing power. CFD simulations of the model in the KWT test section on its pylon and in free air showed very little effects of the pylon / strut on the results and the directional flow field around the tail. This leads to the possibility that wake coming from the dihedral canards is affecting the vertical tail in some way.

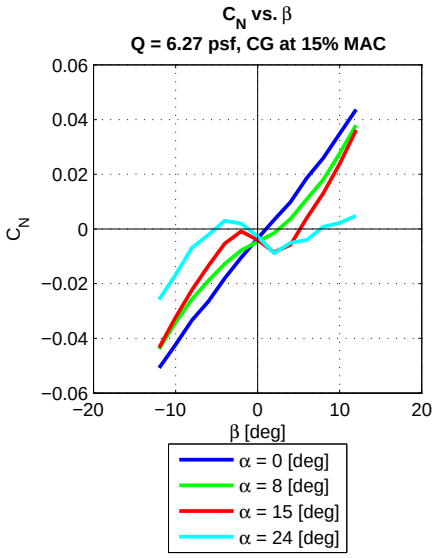

Figure 5.8: Yawing Moment of the Final Configuration at Various Angles of Attack.

The aircraft was also stable in roll, which was much more immune to changes in angle of attack than the yawing stability. In contrast to the static yaw stability, dihedral stability was found to slightly increase with an increase in angle of attack. This can be seen in Figure 5.9.

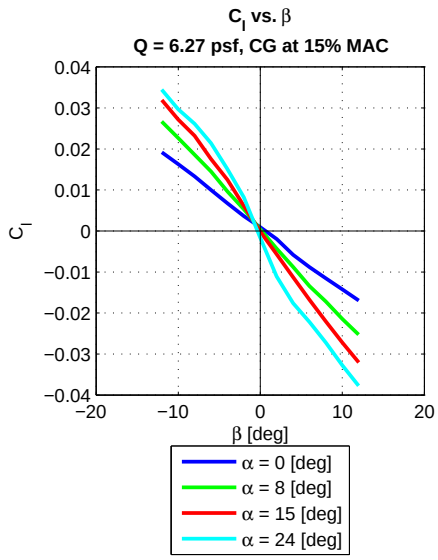

Figure 5.9: Rolling Moment of the Final Configuration at Various Angles of Attack.

5.5 Dynamic Stability

Aerodynamic derivatives due to roll, pitch, yaw rates and the rate of change of angle of attack were determined using the ZAERO code based on a NASTRAN detailed finite element model of the geometry of the R-UAV.

ZAERO also produces static stability derivatives, and those can be checked against the wind tunnel measured ones for experience and insight. Another advantage of the ZAERO capabilities is the modeling of the full size airplane at supersonic flight conditions, which the NASTRAN subsonic Doublet Lattice Method cannot do.

Comparing ZAERO-predicted static stability derivatives with measured results from the wind tunnel on the configuration with full-size vertical tail showed that all longitudinal results were within 10% of the wind tunnel values (Table 5.3). The ZAERO lateral-directional derivatives show significant differences from their wind tunnel measured values, which is not surprising, given the difficulty of all linear aerodynamic panel codes with 3D bodies and the more significant effect of the fuselage relative to lifting surfaces (vertical tail and canards) in the directional case.

Table 5.3: Comparison of Stability Derivatives for the Final Configuration Found with Various Methods (in radians)

Derivative	ZAERO	Wind Tunnel
CL_α	2.834	2.8629
CM_α	-0.265	-0.2672
CD_α	N/A	-0.2666
CY_β	-0.374	-0.638
Cl_β	-0.039	-0.0941
CN_β	0.1	0.1809

Once the ZAERO model was validated, it afforded the opportunity to run many different vertical tail sizes to find the effect on both the static and dynamic derivatives. This allowed for the creation of a MATLAB script that could determine the point, via root-locus analysis, at which reduction of vertical tail size leads to aircraft low-speed dynamic instability by following the changes in the flight dynamic poles of the various corresponding [A] matrices.

ZAERO analyses for stability derivative evaluation were run with the full vertical tail, a 3/4 size vertical tail, a 1/2 vertical tail, and with no vertical tail. The full vertical tail and the no vertical tail configurations were checked against wind tunnel runs.

Figures 5.10, 5.11, 5.12, and 5.13 show the ZAERO model for the various cases analyzed.

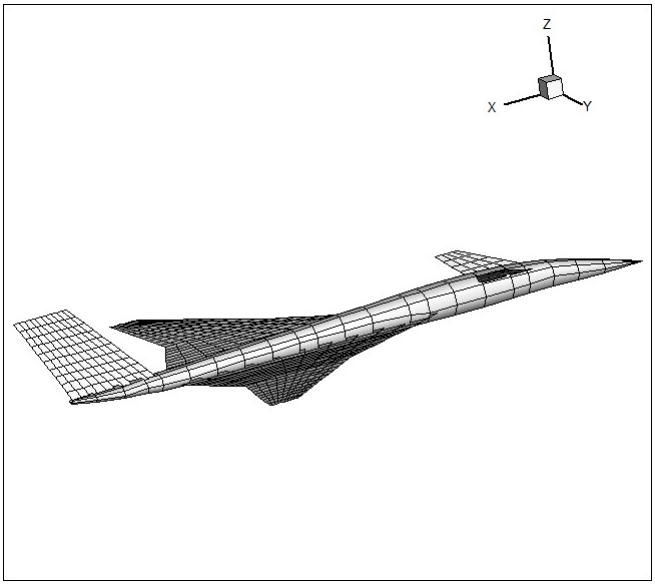

Figure 5.10: ZAERO Model with Full Sized Vertical Tail

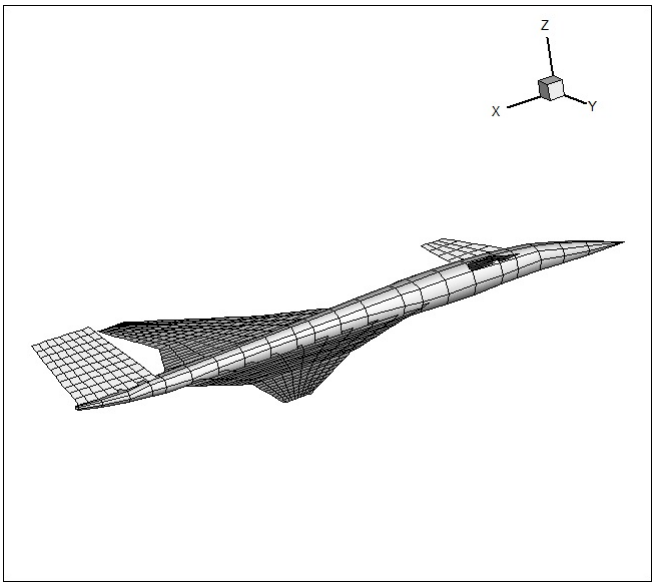

Figure 5.11: ZAERO Model with 3/4 Sized Vertical Tail

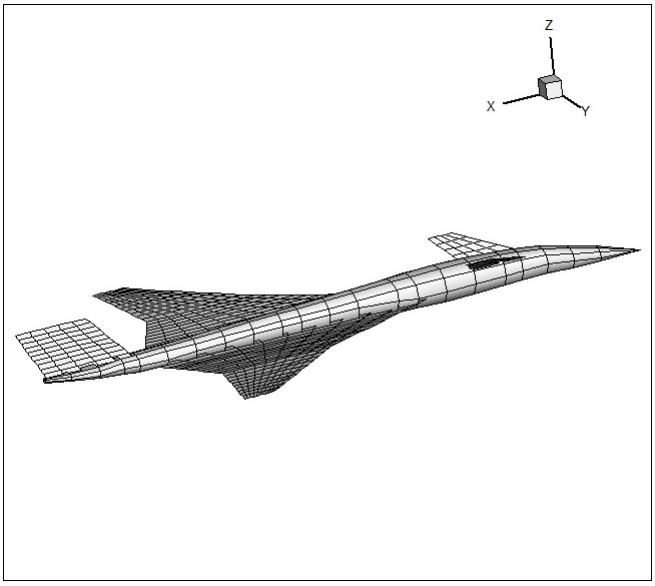

Figure 5.12: ZAERO Model with 1/2 Sized Vertical Tail

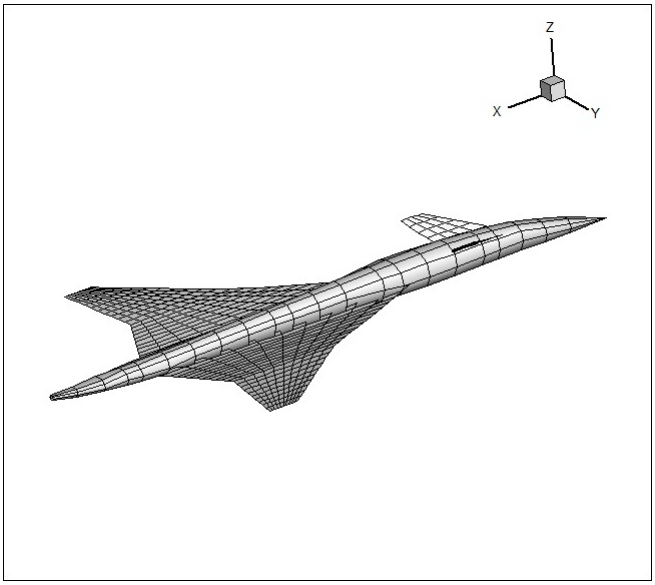

Figure 5.13: ZAERO Model with No Vertical Tail

The dynamic stability derivatives for five different vertical tail sizes are summarized in Table 5.4.

Table 5.4: R-UAV Dynamic Derivatives at Five Different Vertical Tail Sizes.

Tail Size	$CL_{\dot{\alpha}}$ $\frac{\partial C_L}{\partial \dot{\alpha} / 2V}$	CL_q $\frac{\partial C_L}{\partial qc/2V}$	$Cm_{\dot{\alpha}}$ $\frac{\partial C_m}{\partial \dot{\alpha} / 2V}$	Cm_q $\frac{\partial C_m}{\partial qc/2V}$
Full Vertical Tail	1.737	4.698	-0.2836	-3.244
75% Vertical Tail	1.737	4.698	-0.28366	-3.244
50% Vertical Tail	1.737	4.698	-0.2836	-3.244
No Vertical Tail	1.737	4.698	-0.2836	-3.244

Tail Size	CY_r $\frac{\partial C_Y}{\partial rb/2V}$	CY_p $\frac{\partial C_Y}{\partial pb/2V}$	Cl_r $\frac{\partial C_l}{\partial rb/2V}$	Cl_p $\frac{\partial C_l}{\partial pb/2V}$	CN_r $\frac{\partial C_N}{\partial rb/2V}$	CN_p $\frac{\partial C_N}{\partial pb/2V}$
Full Vertical Tail	0.4276	-0.009792	0.1004	-0.210 3	-0.4740	-0.02413
75% Vertical Tail	0.2731	0.004116	0.06996	-0.2075	-0.3503	-0.03501
50% Vertical Tail	0.0952	0.003585	0.04457	-0.2075	-0.2172	-0.03438
No Vertical Tail	-0.1188	-0.04006	0.03082	-0.2096	-0.07843	-0.007207

Comparison of ZAERO derivatives with and without vertical tail to wind tunnel test data is shown in Table 5.5.

Table 5.5: ZAERO and Wind Tunnel Derivative Comparison with and without the Vertical Tail (in radians)

Derivative	ZAERO With Vertical Tail	ZAERO Without Vertical Tail
CL_α	2.834	2.834
CM_α	-0.265	-0.265
CD_α	N/A	N/A
CY_β	-0.374	-0.115
Cl_β	-0.039	-0.00304
CN_β	0.100	-0.08904
CY_r	0.4627	-0.1188
CY_p	-0.009792	-0.04006
Cl_r	0.1004	0.03082
Cl_p	-0.2203	-0.2096
CN_r	-0.4740	-0.07843
CN_p	-0.02413	-0.007207

Derivative	Wind Tunnel With Vertical Tail	Wind Tunnel Without Vertical Tail
CL_α	2.8629	2.869
CM_α	-0.2672	-0.2672
CD_α	-0.2666	-0.2666
CY_β	-0.638	-0.213
Cl_β	-0.0941	-0.0424
CN_β	0.1809	-0.0613

The predicted change is lateral-directional derivatives by ZAERO in comparison to the wind tunnel is shown in Table 5.6.

Table 5.6: Change in Lateral-Directional Derivatives Caused by the Removal of the Vertical Tail (in radians)

Derivative Per Radian	ZAERO Predicted Change	Wind Tunnel Change
CY_β	-0.259	-0.425
Cl_β	-0.03596	-0.0517
CN_β	0.18904	0.2422

A table of relative changes (with respect to the full vertical tail results) is shown in Table 5.7.

Table 5.7: Relative Change in Lateral-Directional Derivatives Caused by the Removal of the Vertical Tail

Derivative Per Radian	ZAERO Predicted Relative Change	Wind Tunnel Change Relative Change
CY_β	69.25%	66.61%
Cl_β	92.2%	54.9%
CN_β	189%	133.9%

Table 5.7 shows percent reduction in stability derivatives (relative to their wind tunnel values at full vertical tail size) due to removal of the vertical tail.

Chapter 6

INERTIAL PROPERTIES

Inertial properties of the 2014 UW R-UAV were determined based on careful component by component weight and balance analysis of the configuration fine-tuned by total weight and center of mass location measurement. The detailed NASTRAN Finite Element model of the R-UAV was used. The total mass of the NASTRANs pure structure model was fine-tuned by the total mass of the pure as-built composite structure of the airframe. Masses and locations of all non-structural parts of the R-UAV were then added to the NASTRAN model, including motors, EDFs, nacelles, landing-gear, servo actuators, and batteries.

The results are summarized in Table 6.1. The structural Finite Element NASTRAN mesh, with and without the vertical tail, can be seen in Figures 6.1 through 6.5.

Table 6.1: Moments of Inertial of the R-UAV (with and without the vertical tail) as Determined by NASTRAN

	Model With Vertical Tail	Model Without Vertical Tail
Mass [lb]	30.9	30.2
X_{cg} [in]	56.1	55.2
Z_{cg} [in]	-1.3	-1.5
Moment	[lb*in^2]	[lb*in^2]
I_{xx}	1383	1327
I_{yy}	9489	8382
I_{zz}	10521	9469
I_{xz}	131	-95

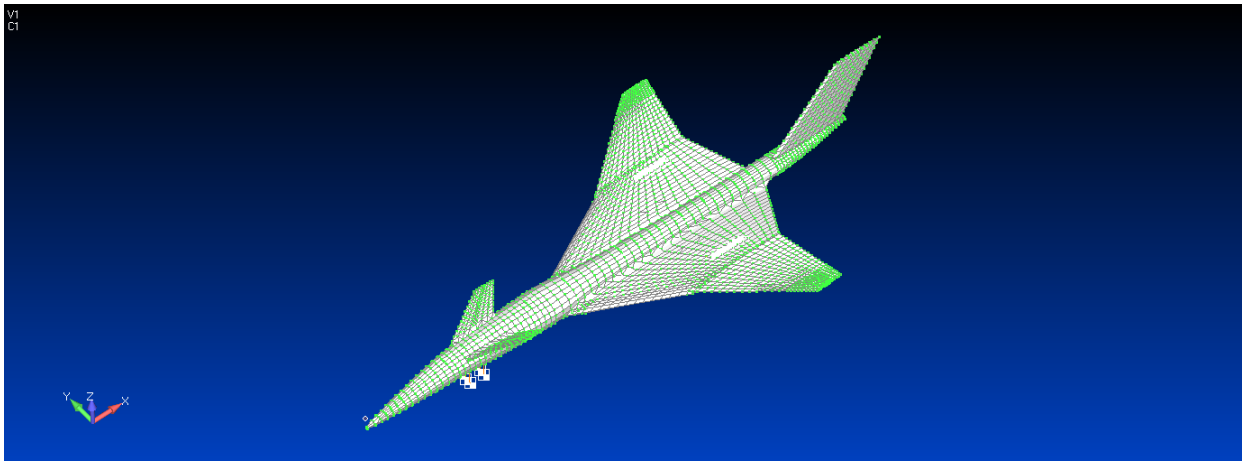

Figure 6.1: Top View of Femap Structural Mesh with the Vertical Tail

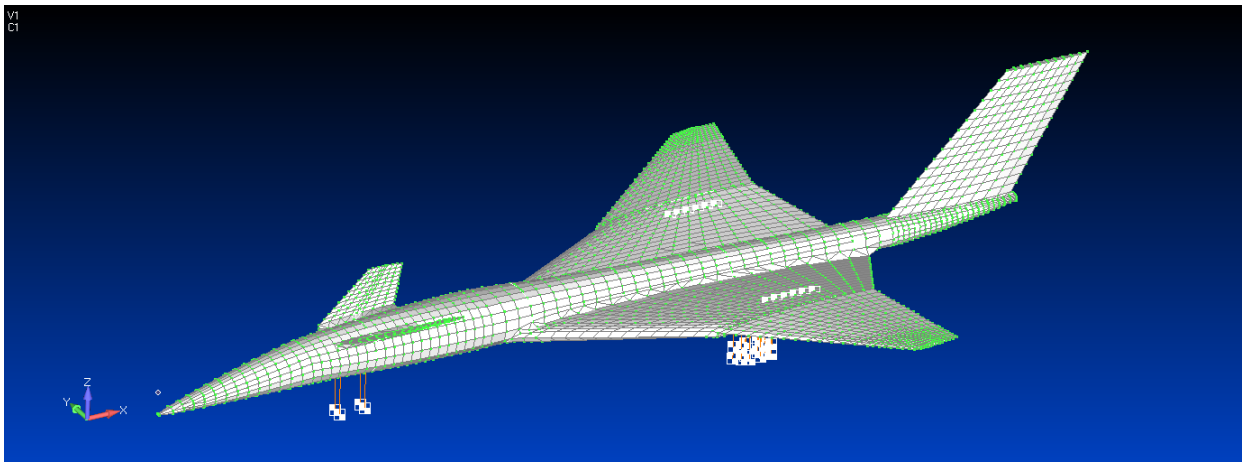

Figure 6.2: Side View of Femap Structural Mesh with the Vertical Tail

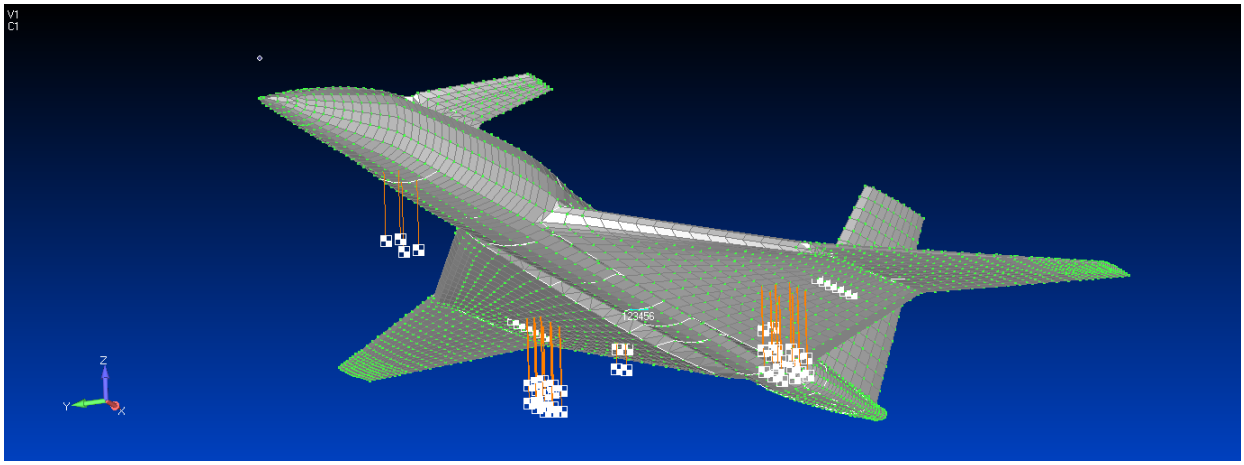

Figure 6.3: Bottom View of Femap Structural Mesh with the Vertical Tail

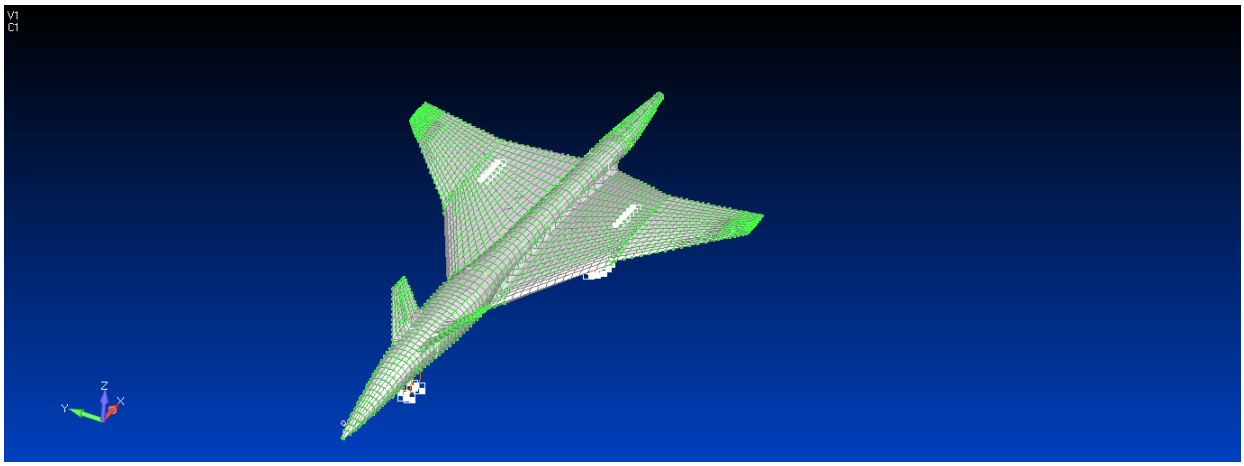

Figure 6.4: Top View of Femap Structural Mesh without the Vertical Tail

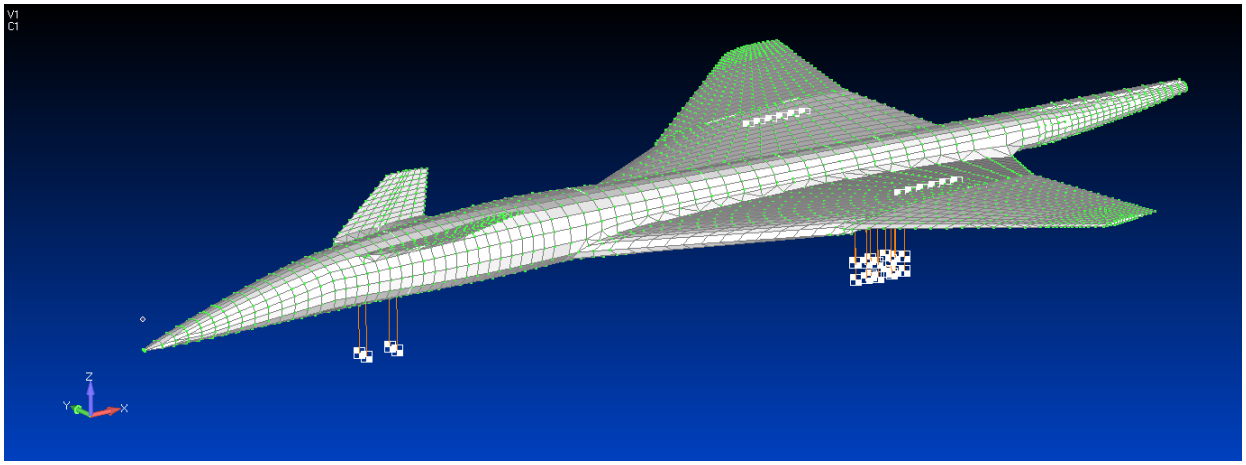

Figure 6.5: Side View of Femap Structural Mesh with the Vertical Tail

The detailed weight & balance NASTRAN model makes it possible to quickly evaluate the effects of configuration changes on the total mass, CG location, and moments of inertia, and as a result the effect of configuration changes on the stability and control of the R-UAV.

This applies to possible external changes (size of tail surfaces, or canards, or no tails or canards) and internal arrangement of systems and payload. To reduce risk and allow focusing on the stability and control challenges it was decided to build the R-UAV with a fixed extended landing gear. The NASTRAN weight & balance model allows quick generation of the inertial properties of the R-UAV with the landing gear retracted.

Chapter 7

FLIGHT DYNAMIC CHARACTERISTICS OF THE 2014 UW R-UAV OPEN LOOP

This chapter discusses the flight dynamic characteristics on the R-UAV based on the LTI State Space models described in the previous chapters. Results in this chapter are for the open-loop R-UAV without any closed-loop active control, not even the rate gyro stability augmentation built for the actual R-UAV. The focus here is on the effects of vertical tail size on the stability in the small (based on linearized small perturbation analysis) with respect to the three flight conditions / configurations of interest described earlier.

7.1 Controllability

Since without a vertical tail the R-UAV is expected to be unstable or marginally stable, the question of controllability using the selected five wing and canard control surfaces described earlier becomes important.

With adequate controllability, the vehicle can be stabilized using active control.

To study the controllability of the R-UAV with its selected control surfaces, the state space equations are decoupled by a transformation to modal form. The system is controllable (inputs can reach and affect all states) if all rows of the new [B] matrix or vector are non-zero.

A brief description of this approach follows:

Where $[A]$ is the system's matrix and $[V]$ the matrix of eigenvectors of $[A]$, and with $[B]$ being the input-to-states influence matrix

The system can be transformed from states $\{x\}$ to states $\{\tilde{x}\}$ Using

$$\{x\} = [V]\{\tilde{x}\} \tag{7.1}$$

Leading to

$$\{\frac{d\tilde{x}}{dt}\} = [\tilde{A}]\{\tilde{x}\} + [\tilde{B}]\{\delta\} \tag{7.2}$$

Where

$$[\tilde{A}] = [V]^{-1} * [A] * [V] \tag{7.3}$$

and

$$[\tilde{B}] = [V]^{-1} * [B] \tag{7.4}$$

The new $[\tilde{A}]$ matrix is diagonal. Hence if each row of $[\tilde{B}]$ has at least one non-zero element then all the states of the system can be effected by the inputs.

For the flight conditions and configurations studied and with the control surfaces selected, the R-UAV was found to be controllable in both the longitudinal and lateral-directional cases.

The following equations show the decoupled state space models for the R-UAV at the flight conditions studied. Examination of the transformed [B] matrices sheds some light on the relative effectiveness of different control surface motions on the different states.

Note that the effectiveness of control surface motions studied here is not influenced by the size of the vertical tail and these solutions represent the R-UAV with the full size vertical tail.

Longitudinal

High Speed Cruise Condition

$$\frac{d}{dt}\begin{Bmatrix} u\tilde{/}V \\ \tilde{\alpha} \\ \tilde{q} \\ \tilde{\theta} \end{Bmatrix} = \begin{bmatrix} -5.08+7.95i & 0 & 0 & 0 \\ 0 & -5.08-7.95i & 0 & 0 \\ 0 & 0 & -0.05+0.23i & 0 \\ 0 & 0 & 0 & -0.05-0.23i \end{bmatrix} \begin{Bmatrix} u\tilde{/}V \\ \tilde{\alpha} \\ \tilde{q} \\ \tilde{\theta} \end{Bmatrix} + \begin{bmatrix} -50.1-5.88i \\ -50.1+5.88i \\ 3.01-0.58i \\ 3.01+0.58i \end{bmatrix} \delta \tag{7.5}$$

Low Speed Flight Condition

$$\frac{d}{dt}\begin{Bmatrix} u\tilde{/}V \\ \tilde{\alpha} \\ \tilde{q} \\ \tilde{\theta} \end{Bmatrix} = \begin{bmatrix} -2.07+2.12i & 0 & 0 & 0 \\ 0 & -2.07-2.12i & 0 & 0 \\ 0 & 0 & -0.02+0.53i & 0 \\ 0 & 0 & 0 & -0.02-0.53i \end{bmatrix} \begin{Bmatrix} u\tilde{/}V \\ \tilde{\alpha} \\ \tilde{q} \\ \tilde{\theta} \end{Bmatrix} + \begin{bmatrix} 3.86+0.37i \\ 3.86-0.37i \\ 1.04-0.05i \\ 1.04+0.05i \end{bmatrix} * \delta \tag{7.6}$$

Low Speed Flight Flaps Down Condition

$$\frac{d}{dt}\begin{Bmatrix} u/V \\ \tilde{\alpha} \\ \tilde{q} \\ \tilde{\theta} \end{Bmatrix} = \begin{bmatrix} -2.01+1.80i & 0 & 0 & 0 \\ 0 & -2.01-1.80i & 0 & 0 \\ 0 & 0 & 4.0e-4+0.52i & 0 \\ 0 & 0 & 0 & 4.0e-4-0.52i \end{bmatrix} \begin{Bmatrix} u/V \\ \tilde{\alpha} \\ \tilde{q} \\ \tilde{\theta} \end{Bmatrix} + \begin{bmatrix} 4.12+0.38i \\ 4.12-0.38i \\ 1.31-0.13i \\ 1.31+0.13i \end{bmatrix} * \delta \tag{7.7}$$

Where δ is $\delta_{elavator} + \delta_{canard}$ mixed in a 1:1 ratio for all conditions.

Lateral-Directional

High Speed Cruise Condition

$$\frac{d}{dt}\begin{Bmatrix} \tilde{\beta} \\ \tilde{p} \\ \tilde{\phi} \\ \tilde{r} \end{Bmatrix} = \begin{bmatrix} -11.11 & 0 & 0 & 0 \\ 0 & -1.25+8.37i & 0 & 0 \\ 0 & 0 & -1.25-8.37i & 0 \\ 0 & 0 & 0 & -0.20 \end{bmatrix} \begin{Bmatrix} \tilde{\beta} \\ \tilde{p} \\ \tilde{\phi} \\ \tilde{r} \end{Bmatrix} + \begin{bmatrix} 1.79e2 & 59.1 & 50.6 \\ 2.30-13.5i & -6.78-15.6i & -40.4-53.8i \\ 2.30+13.5i & -6.78+15.6i & -40.4+53.8i \\ 19.9 & 8.89 & 15.8 \end{bmatrix} * \{\delta\} \tag{7.8}$$

Low Speed Flight Condition

$$\frac{d}{dt}\begin{Bmatrix}\tilde{\beta}\\ \tilde{p}\\ \tilde{\phi}\\ \tilde{r}\end{Bmatrix} = \begin{bmatrix}-5.87 & 0 & 0 & 0\\ 0 & 0.69+3.58i & 0 & 0\\ 0 & 0 & 0.69-3.58i & 0\\ 0 & 0 & 0 & -0.76\end{bmatrix}\begin{Bmatrix}\tilde{\beta}\\ \tilde{p}\\ \tilde{\phi}\\ \tilde{r}\end{Bmatrix} + \begin{bmatrix}16.6 & 4.70 & 22.6\\ 6.46+4.55i & 0.37-1.80i & -4.11-15.9i\\ 6.46-4.55i & 0.37+1.80i & -4.11+15.9i\\ -0.29 & 2.28 & 16.9\end{bmatrix} * \{\delta\} \tag{7.9}$$

Low Speed Flight Flaps Down Condition

$$\frac{d}{dt}\begin{Bmatrix}\tilde{\beta}\\ \tilde{p}\\ \tilde{\phi}\\ \tilde{r}\end{Bmatrix} = \begin{bmatrix}-5.69 & 0 & 0 & 0\\ 0 & 0.67+3.51i & 0 & 0\\ 0 & 0 & 0.67-3.51i & 0\\ 0 & 0 & 0 & -0.73\end{bmatrix}\begin{Bmatrix}\tilde{\beta}\\ \tilde{p}\\ \tilde{\phi}\\ \tilde{r}\end{Bmatrix} + \begin{bmatrix}15.9 & 4.24 & 20.0\\ 6.06+3.90i & 0.35-1.60i & -3.71-14.2i\\ 6.06-3.90i & 0.35+1.60i & -3.71+14.2i\\ 0.12 & 2.07 & 15.2\end{bmatrix} * \{\delta\} \tag{7.10}$$

Where $\{\delta\} = \begin{bmatrix}\delta_{Flaperon}\\ \delta_{DragRudder}\\ \delta_{DiferentialCanard}\end{bmatrix}$ for all conditions.

It should be noted that the phugoid mode is slightly unstable in the low-speed, flaps down condition. The is highly damped and is considered very much within the pilot's ability to correct. It was not seen as a critical instability. It can also be seen, that even with the full size vertical tail, the aircraft is unstable in dutch roll as both

low-speed conditions. This will be remedied with roll and yaw dampers, and discussed in detail later.

7.2 The Effect of the Vertical Tail

Some discussion of the effect of the vertical tail on various aerodynamic derivatives was presented earlier in the chapter that described the way all stability derivatives for the state space model of the R-UAV were obtained. See Section 5.5.

The incremental vertical tail effects on each derivative are summarized in Tables 7.1 and 7.2 for different angles of attack. The static derivatives were obtained directly from wind tunnel data, while the dynamic derivatives were taken from ZAERO data. The slight discrepancies in these values from the values listed in Tables 5.5 and 5.6 stems from the linearizaton about specific angles of attack.

Table 7.1: Vertical Tail Effect on Lateral-Directional Static Stability Derivatives for Various Angles of Attack.

Derivative	Increment Due to Vertical Tail [per Radian]				
	$\alpha 0°$	$\alpha 8°$	$\alpha 15°$	$\alpha 24°$	$\alpha 35°$
CY_β	-0.52196	-0.1885	0.058442	0.292208	0.43373
Cl_β	-0.03782	-0.02063	-0.00516	-0.07506	-0.1409476
CN_β	0.258977	0.175898	0.169596	0.07563	-0.1409476

Table 7.2: Vertical Tail Effect on Lateral-Directional Dynamic Stability Derivatives (Note - for all angles of attack).

Derivative	Increment Due to Vertical Tail
CY_r	-0.5464
Cl_r	-0.06958
CN_r	0.39557
CY_p	-0.030331
Cl_p	0.017
CN_p	0.016923

The stability of the configuration at various flight conditions can be evaluated by examination of the poles of the state space models of the configuration in both the longitudinal and lateral-directional state spaces.

Figures 7.1 through 7.3 show that the configuration with full size vertical tail is longitudinally stable at all flight conditions with the exception of the low-speed, flaps extending case being unstable in the phugoid mode. This instability, because of the very long period and slow rate of divergence is well within the pilot's ability to correct by hand.

It was found that the vertical tail did not have an effect on the longitudinal dynamics of the aircraft. Only the full-sized vertical tail case is, therefore, shown on the longitudinal plots.

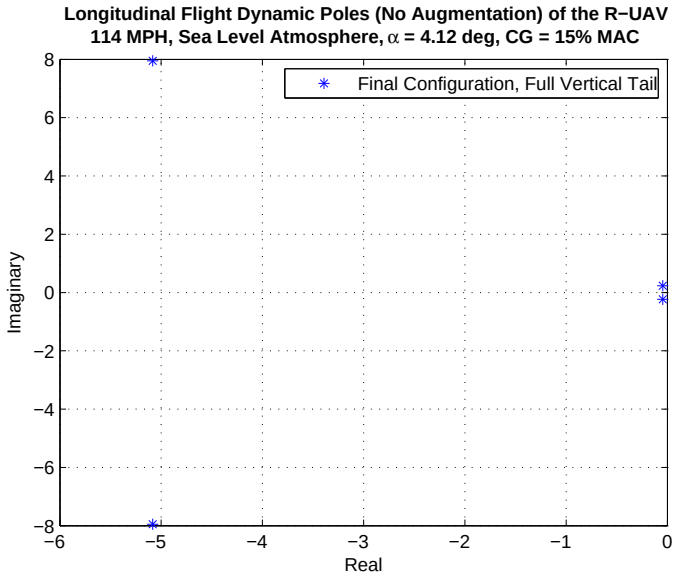

Figure 7.1: Longitudinal Dynamic Poles of the R-UAV at Cruise.

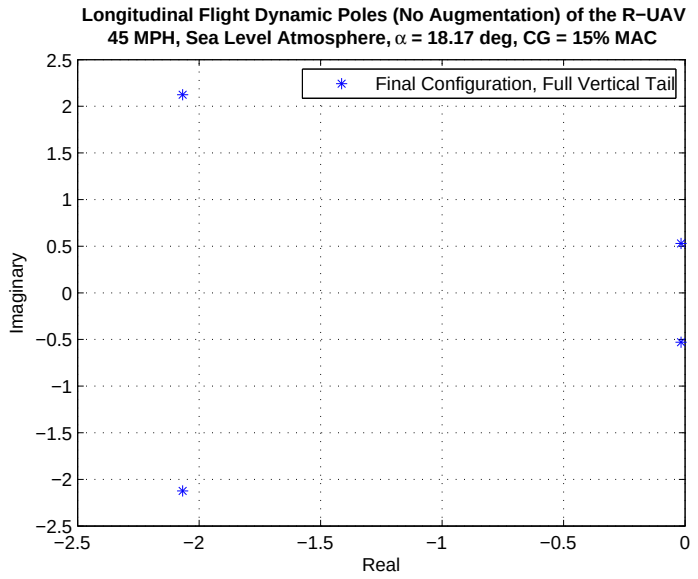

Figure 7.2: Longitudinal Dynamic Poles of the R-UAV at Low-Speed Flight.

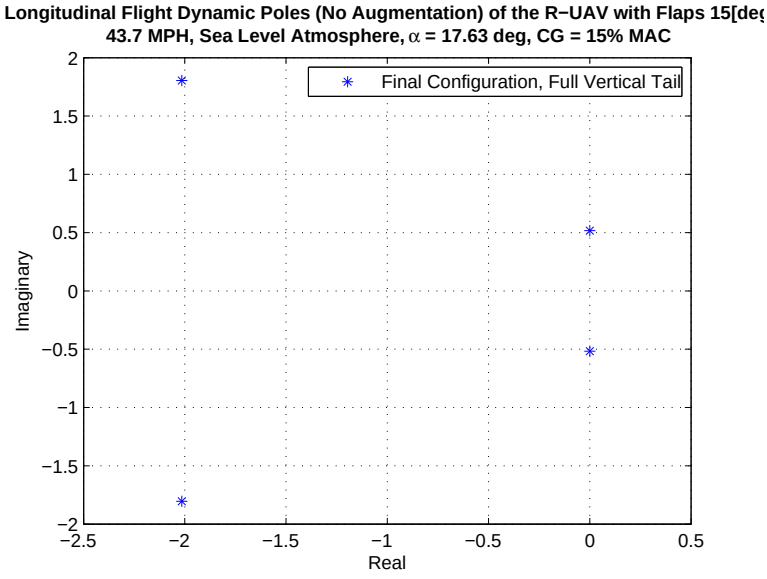

Figure 7.3: Longitudinal Dynamic Poles of the R-UAV at Take-Off and Landing Conditions.

The damping ratios and natural frequencies for all longitudinal cases are listed in

Table 7.3.

Table 7.3: Damping Ratios and Natural Frequencies for All Longitudinal Flight Conditions

Flight Condition	Pole	Natural Frequency (rads/sec)	Damping Ratio
High	-5.08 +/- 7.95i	9.44	0.54
Speed	-0.05 +/- 0.23i	0.24	0.19
Low	-2.01 +/- 2.12i	2.96	0.70
Speed	-0.02 +/- 0.53i	0.53	0.03
Low			
Speed	-2.01 +/- 1.80i	2.70	0.71
Flaps	4.0e-4 +/- 0.52i	0.52	-7.0e-4

For the lateral-directional case Figures 7.4 through 7.6 show the deteriorating stability of the R-UAV as the vertical tail size is reduced. It is clear from the plots that the spiral and roll stability modes, while worsening with reduction of the vertical tail area, do not pose significant risks, as they stay stable at all flight conditions. However, it can be seen in figures 7.5 and 7.6 that the dutch roll stability mode is unstable at all flight conditions, with the damping becoming progressively worse as the vertical tail area is reduced. This is quite expected for a double-delta slender configuration, such as the one studied here, without a vertical tail but even with a vertical tail if it is too small.

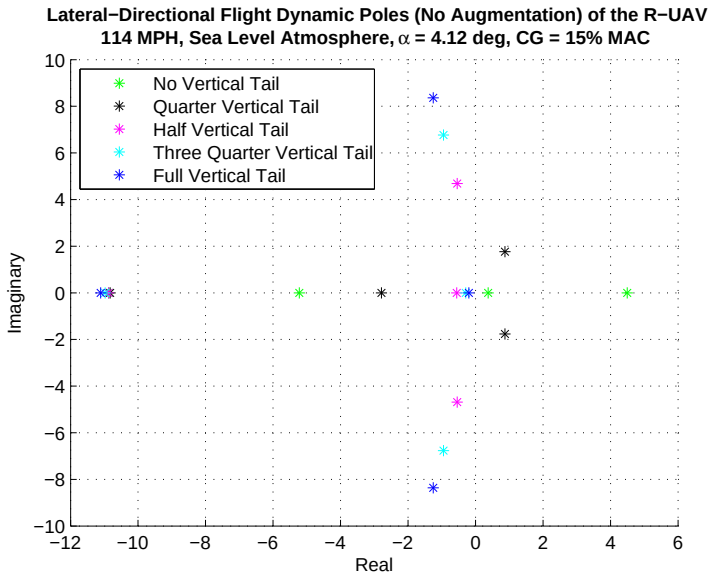

Figure 7.4: Lateral-Directional Dynamic Poles of the R-UAV at Cruise.

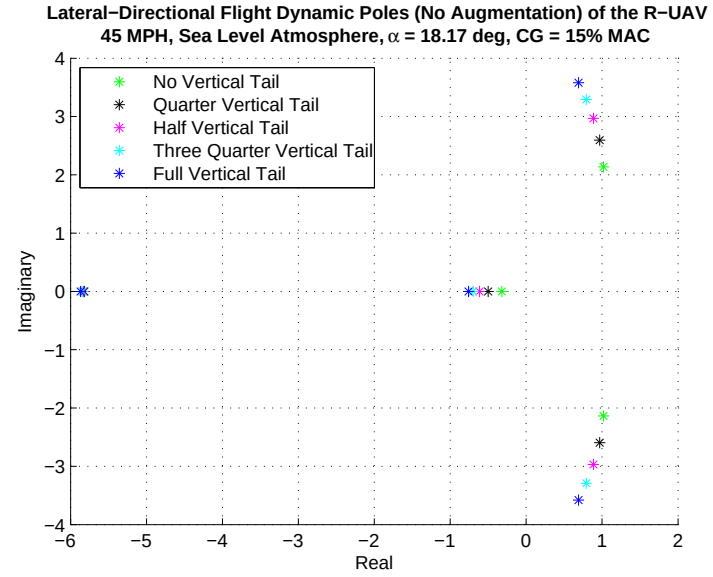

Figure 7.5: Lateral-Directional Dynamic Poles of the R-UAV at Low-Speed Flight.

Note - The tailless configuration at this flight condition was found to be on the

boundary of the oscillatory region, with three real poles produced rather than the expected two real and one complex conjugate pole.

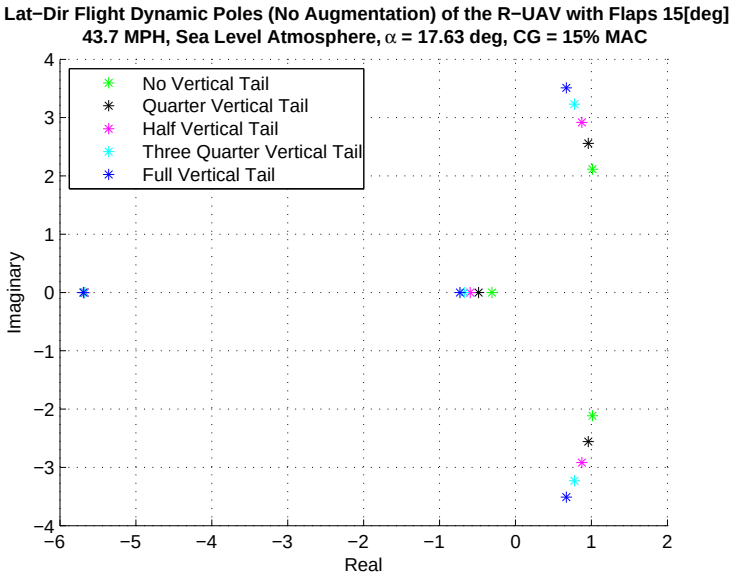

Figure 7.6: Lateral-Directional Dynamic Poles of the R-UAV at Take-Off and Landing Conditions.

Tables 7.4, 7.5, and 7.6 list the numerical values of the lateral-directional poles for the three flight conditions studied and for the various vertical tail sizes studied.

Table 7.4: Lateral-Directional Poles for High Speed Cruise Flight at Various Vertical Tail Sizes

% Vertical Tail	Pole	Natural Frequency (rad/sec)	Damping Ratio
100%	-11.1	11.1	–
	-1.25 +/- 8.37i	8.46	0.15
	-0.20	0.20	–
75%	-10.97	10.97	–
	-0.951 +/- 6.77i	6.84	0.14
	-0.288	0.288	–
50%	-10.87	10.87	–
	-0.544 +/- 4.68i	4.72	0.12
	-0.557	0.557	–
25%	-10.83	10.83	–
	0.872 +/- 1.77i	1.97	-0.44
	-2.79	2.79	–
0%	-10.87	10.87	–
	4.50	4.50	–
	-5.22	5.22	–
	0.373	0.373	–

Table 7.5: Lateral-Directional Poles for Low Speed Flight at Various Vertical Tail Sizes

% Vertical Tail	Pole	Natural Frequency (rad/sec)	Damping Ratio
100%	-5.87	5.87	–
	0.69 +/- 3.58i	3.65	-0.19
	-0.76	0.76	–
75%	-5.85	5.85	–
	0.79 +/- 3.29i	3.37	-0.23
	-0.70	0.70	–
50%	-5.83	5.83	–
	0.89 +/- 2.97i	3.10	-0.29
	-0.61	0.61	–
25%	-5.82	5.82	–
	0.97 +/- 2.59i	2.77	-0.35
	-0.50	0.50	–
0%	-5.82	5.82	–
	1.02 +/- 2.14	2.37	-0.43
	-0.32	0.32	–

Table 7.6: Lateral-Directional Poles for Low Speed Flight with Flaps at Various Vertical Tail Sizes

% Vertical Tail	Pole	Natural Frequency (rad/sec)	Damping Ratio
100%	-5.69	5.69	–
	0.67 +/- 3.51i	3.57	-0.19
	-0.73	0.73	–
75%	-5.68	5.68	–
	0.76 +/- 3.23i	3.32	-0.23
	-0.67	0.67	–
50%	-5.67	5.67	–
	0.87 +/- 2.92i	3.05	-0.29
	-0.60	0.60	–
25%	-5.67	5.67	–
	0.96 +/- 2.56i	2.73	-0.35
	-0.49	0.49	–
0%	-5.68	5.68	–
	1.01 +/- 2.12	2.35	-0.43
	-0.31	0.31	–

Note that Dutch Roll instability in large, swept-wing transports can usually be eliminated by the incorporation of a yaw-damper, using the rudder in conventional aircraft. It was found with this configuration that a yaw damper alone was insufficient, and a roll damper must also be present in the insufficient or no-vertical-tail cases here.

Chapter 8

FLIGHT DYNAMIC CHARACTERISTICS OF THE 2014 UW R-UAV CLOSED LOOP

8.1 Yaw Damper and Roll Damper

The yaw damper [16] is a device that converts measured yaw rate (obtained from a yaw rate gyro) to a rudder command proportional to it. The effect is to increase the damping of the Dutch-Roll mode, primarily on swept-wing transport type aircraft. The roll damper is a device analogous to the yaw damper, that instead drives the roll control surfaces. This is used to damp out the rolling motion associated with the Dutch-Roll mode, common with the low aspect ratio style of aircraft.

Focusing on one of the flight conditions studied here, in an exploratory effort to evaluate yaw dampers and roll dampers as means for stabilizing the R-UAV in lateral-directional motion, the most unstable Dutch-Roll case is studied. The low speed flight condition was shown to be most unstable, and therefore was chosen for study. Flaps were not considered.

Once a yaw control surface is selected, implementation of a yaw damper is straightforward and is described in Ref [16] pp. 237-241. A brief derivation of a yaw damper with pilot input follows:

$$\{\dot{x}\} = [A]\{x\} + \{B_r\}(\delta_{rF}) + \{B_r\}(\delta_{rp}) \tag{8.1}$$

$$\delta_{rF} = -[K]\{x\} \tag{8.2}$$

$$\{\dot{x}\} = [A - B_R K]\{x\} + \{B_r\}\delta_{rp} \tag{8.3}$$

Where:

$\{x\}$ = the lateral-directional state vector

$[A]$ = the unaugmented plant matrix

$\{B_R\}$ = the rudder control effectiveness column vector

$[K]$ = the feedback row vector

δ_{rp} = the pilot input command to rudder control

δ_{rF} = the feedback input command to rudder control

$[A - B_R K]$ = the augmented plant matrix

The roll damper is derived in the same manner by replacing the rudder control device with the roll control device.

Selecting the differential canard first to be the yaw control device and the flaperon to be the roll control device, a Dutch Roll gain matrix of Kr and Kp is used and varied to achieve a stable airplane in lateral-directional motion. Figure 8.1 is a root locus of the lateral-directional poles showing the changes in the poles due to changes in gain Kr and Kp. For simplicity, it was kept that $Kr = Kp$. From this plot, it was decided that a gain of -0.4 should be used as a safe starting point for flight test. Figure 8.2 shows the state response to a 1 degree sideslip angle with a both yaw and roll dampers implemented and set to a gain of -0.4.

Without pilot commands the equations with both a yaw and roll damper implemented become:

$$\{\dot{x}\} = [A]\{x\} + \{B_r\}(\delta_r) + \{B_p\}(\delta_p) \tag{8.4}$$

$$\delta_r = -\begin{bmatrix} 0 & 0 & 0 & K_r \end{bmatrix}\{x\} = -[K_r]\{x\} \tag{8.5}$$

$$\delta_p = -\begin{bmatrix} 0 & K_p & 0 & 0 \end{bmatrix}\{x\} = -[K_p]\{x\} \tag{8.6}$$

$$\{\dot{x}\} = [A - B_r[K_r] - B_p[K_p]]\{x\} \tag{8.7}$$

Where:

$\{x\}$ = the lateral-directional state vector

$[A]$ = the unaugmented plant matrix

$\{B_r\}$ = the yaw control effectiveness column vector

$\{B_p\}$ = the roll control effectiveness column vector

$\{\delta_r\}$ = the feedback input command to rudder control

$\{\delta_p\}$ = the feedback input command to roll control

$[K_r]$ = the yaw feedback row vector

$[K_p]$ = the roll feedback row vector

$[A - \{B_r\}[K_r] - \{B_p\}[K_p]]$ = the augmented plant matrix

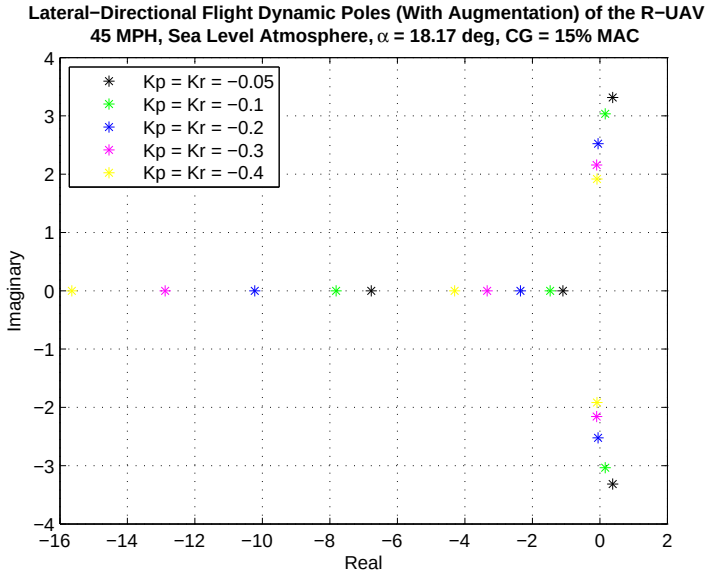

Figure 8.1: Root Locus Plot of the Lat-Dir R-UAV Poles at Various Yaw and Roll Damper Gains

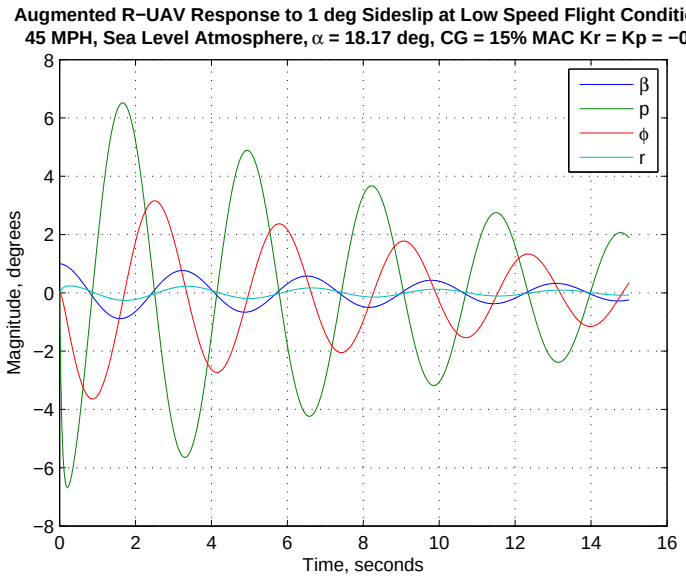

Figure 8.2: Time History of Damper Augmented R-UAV to a 1 Degree Sideslip Angle

The figures show that simple yaw-damper and roll-damper control using the available yaw control and roll control devices on the R-UAV is capable of stabilizing the R-UAV in lateral-directional motion in the worst open-loop combination of flight conditions and full vertical tail size.

It was also studied if the simple combination of yaw and roll dampers could stabilize the tailless aircraft at both the high-speed and low-speed flight conditions. It was determined that it was possible to stabilize the tailless aircraft in high-speed cruise using 10 times the full-sized vertical tail gains and possible to stabilize the tailless aircraft at low-speed conditions with 100 times the full-sized vertical tail gains.

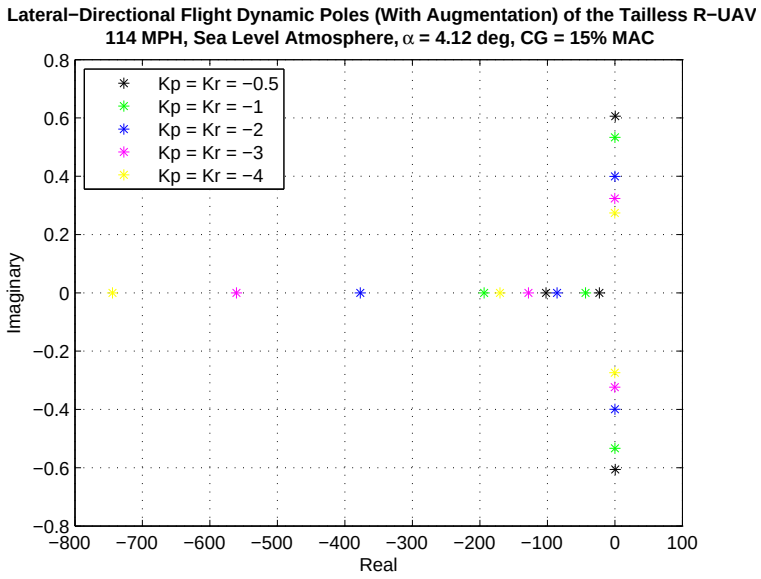

Figure 8.3: Root Locus Plot of the Lat-Dir Tailless R-UAV Poles at Various Yaw and Roll Damper Gains

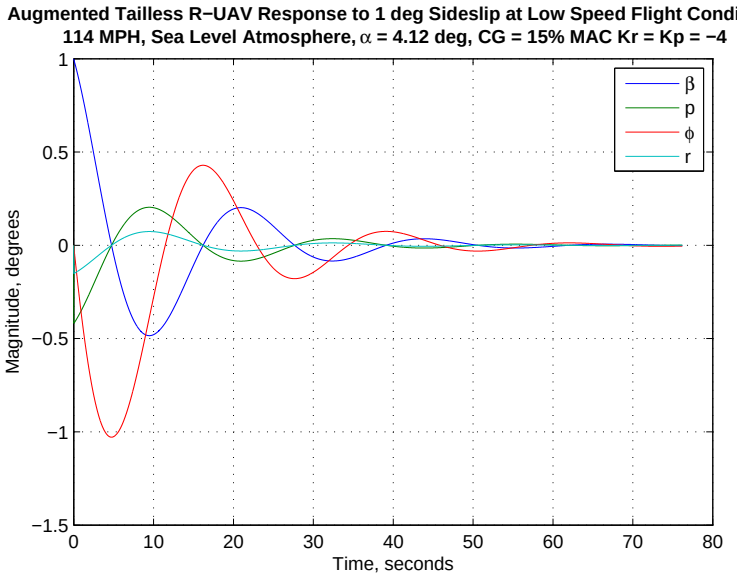

Figure 8.4: Time History of Damper Augmented Tailless R-UAV to a 1 Degree Sideslip Angle

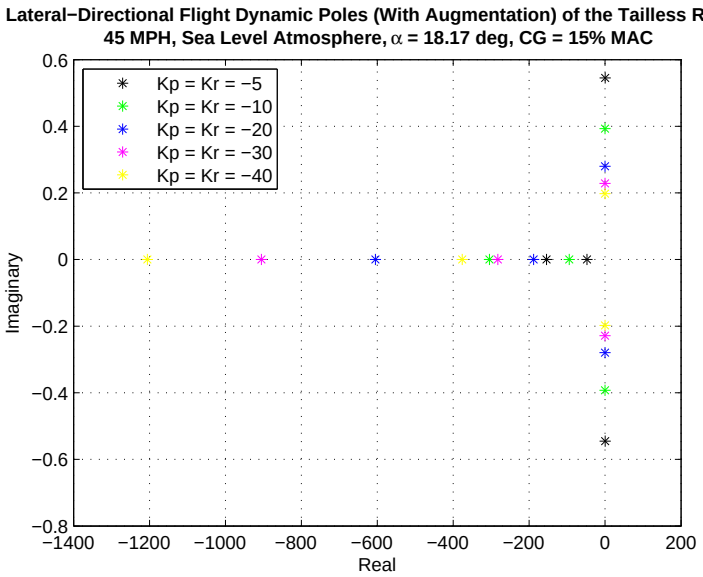

Figure 8.5: Root Locus Plot of the Lat-Dir Tailless R-UAV Poles at Various Yaw and Roll Damper Gains

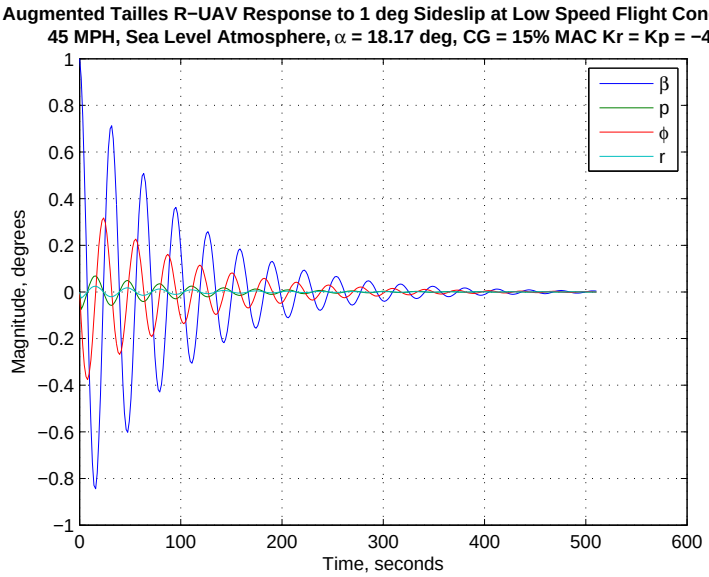

Figure 8.6: Time History of Damper Augmented Tailless R-UAV to a 1 Degree Sideslip Angle

Figures 8.4 and 8.6 show that while the tailless R-UAV is stable, the time-scale is such that it is not a practical way to stabilize the aircraft, and thus a more complex controller is required for the R-UAV with the vertical tail completely removed.

8.2 LQR

Considerable trial and error may be required to find the best combination of yaw control devices that would work effectively with a yaw damper type of controller to stabilize the configuration in lateral-directional motion, or a combination of rate gyros driving different surfaces. A Linear Quadratic Regulator (LQR), being inherently suitable for Multi-Input Multi-Output (MIMO) system controller design, would offer valuable insights regarding the relative effectiveness and action of the various control inputs available and how to best use them.

A steady-state LQR controller, in the case of a controllable linear system, minimizes the error of a quadratic cost functional of the form:

$$J = 1/2 \int_0^\infty (x(t)^T Q(t) x(t) + u(t)^T R(t) u(t)) dt \tag{8.8}$$

The equations for the state feedback controller that would minimize this functional have been derived over the years in a number of ways. References [21] and [22] both give detailed derivations. The presentation and discussion of the LQR controller, its properties, advantages and disadvantages, have all been included in numerous publications and will not be repeated here.

Selection of the weight matrices [Q] and [R] assigns more or less relative weight to the states and inputs affecting the functional. The [Q] matrix, through determining the relative effects of the states on the functional, affects the rate by which the states of the closed-loop system would decay to zero after an initial conditions disturbance. The [R] matrix, assigning weight to the effects of the control inputs, determines the importance of the control effort involved in controlling the system. By changing the

[Q] and [R] matrices the poles of the closed-loop system can be moved to desired locations and the control effort may be brought to desired levels. For the exploratory studies here it was decided that [Q] and [R] would both be identity matrices, giving equal weight to all the states and control surfaces.

Closed-loop LQR was implemented using MATLAB for the R-UAV to see if without its vertical tail it could be reasonably controlled. Time histories of the response of the LQR controlled vehicle to an initial condition of a 1 degree sideslip angle are shown in the following figures.

As is seen in Figure 8.7 the unagumented aircraft at cruise is very unstable, diverging in motion after a start from the initial condition selected in less than 3 seconds. The LQR closed-loop controller stabilizes the closed-loop system as can be seen in Figure 8.8. To study the level of activity of the various lateral-directional control surfaces used for the LQR control the time histories of control surface motions due to an initial condition disturbance of a 1 degree sideslip angle are shown in Figure 8.9.

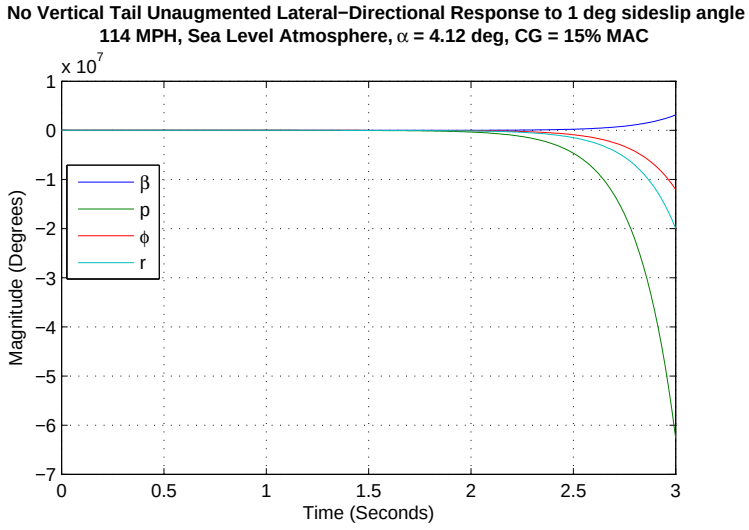

Figure 8.7: State Response of the R-UAV without a Vertical Tail to a Sideslip Angle

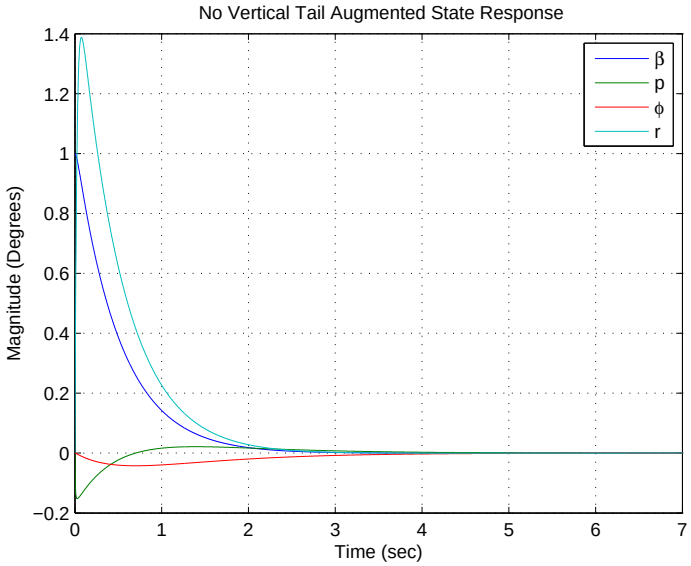

Figure 8.8: State Response of the R-UAV without a Vertical Tail with LQR Control Implemented

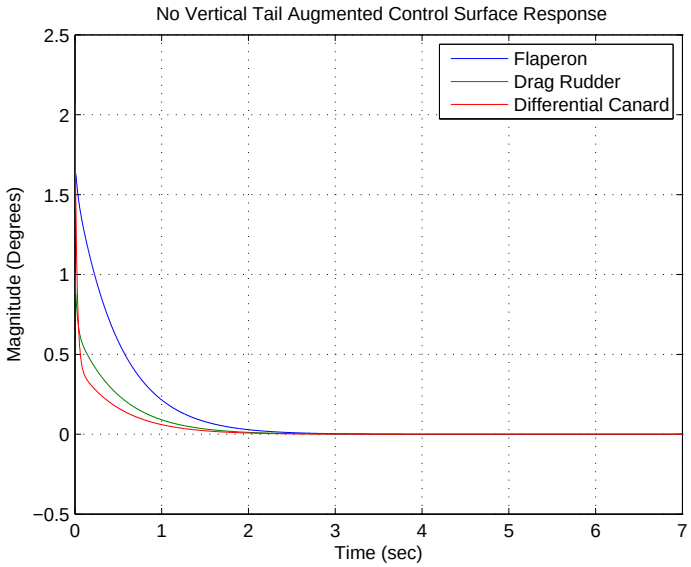

Figure 8.9: Control Surface Responses Required to Stabilize Tailless R-UAV from the above State Response

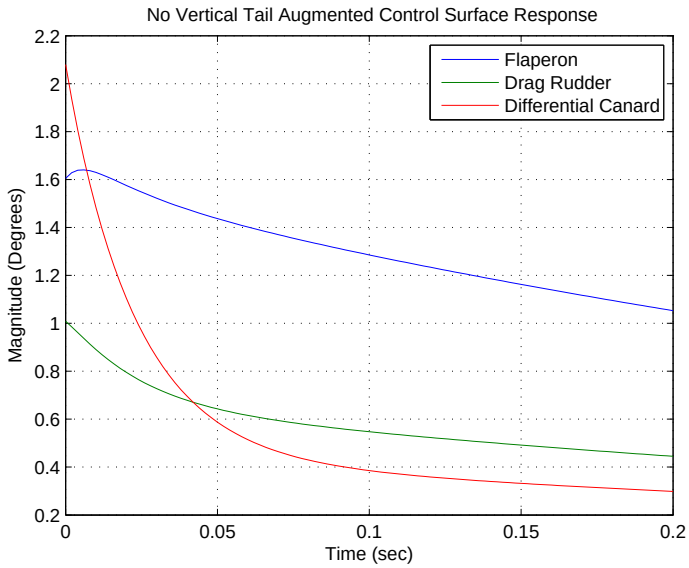

Figure 8.10: Control Surface Responses Required from 0 - 0.2 Seconds to Stabilize Tailless R-UAV

From Figures 8.9 and 8.10 it can be inferred that a combination of differential canard and flaperon are the most important control surfaces necessary to stabilize the aircraft. Each surface deflects by similar amounts and, therefore, it is likely that combination of a yaw damper on the differential canard and a roll damper on the flaperon will have the most beneficial effect for stabilizing the R-UAV. The total control surface deflections shown in Figures 8.9 and 8.10 are also reasonable for the R-UAV scale. However, the rates at which the deflections much occur are suspect. It is uncertain if the current actuators available for an R-UAV would have the necessary rate or bandwidth (the ability to change directions) to fully stabilize the aircraft. Translating this to the full-scale design, the overall control surface deflections would decrease, leading to very reasonable results - however the rates and bandwidths required by the actuators would still be very limiting. However, for the full scale aircraft, specific actuators could be designed to meet these requirements.

For completeness - it was confirmed that LQR was able to stabilize the aircraft in

a similar manner for the two other key flight conditions studied, low-speed flaps up and low-speed flaps down. As the flaps did not have a large lateral-directional effect, the two cases were very similar.

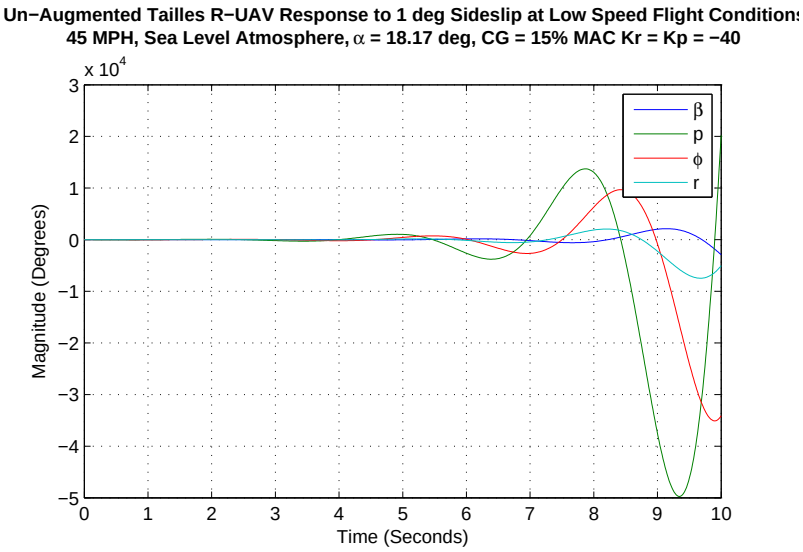

Figure 8.11: State Response of the R-UAV without a Vertical Tail to a Sideslip Angle

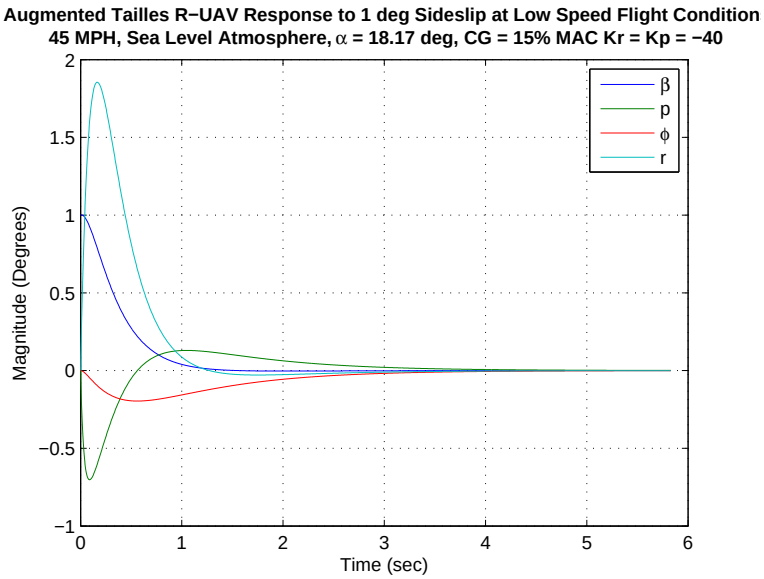

Figure 8.12: State Response of the R-UAV without a Vertical Tail with LQR Control Implemented

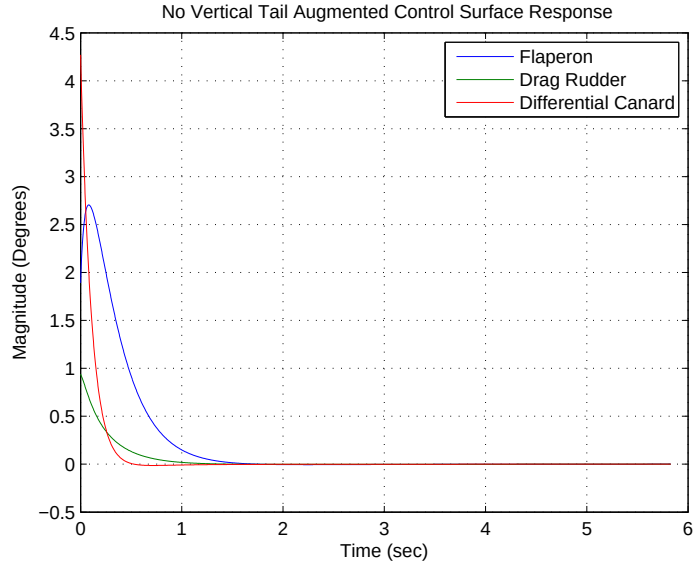

Figure 8.13: Control Surface Responses Required to Stabilize Tailless R-UAV from the above State Response

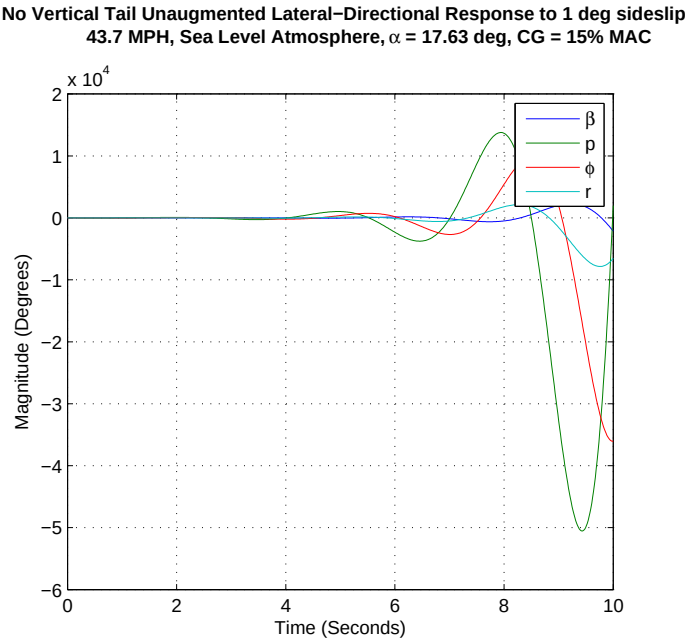

Figure 8.14: State Response of the R-UAV without a Vertical Tail to a Sideslip Angle

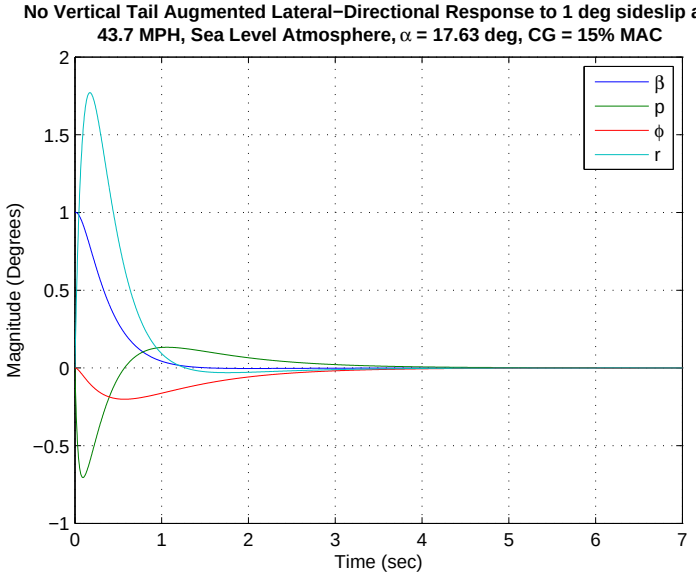

Figure 8.15: State Response of the R-UAV without a Vertical Tail with LQR Control Implemented

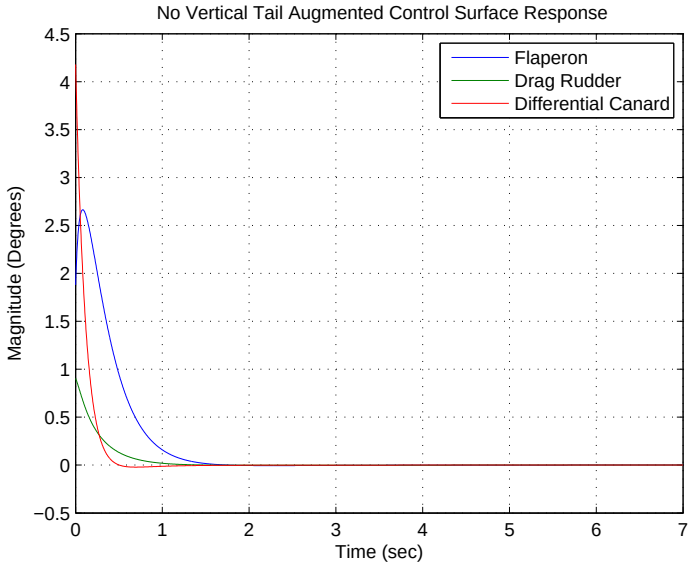

Figure 8.16: Control Surface Responses Required to Stabilize Tailless R-UAV from the above State Response

From Figures 8.11 and 8.14 it can be inferred that the open-loop stability of the tailless R-UAV at these low-speed conditions is so unstable that the magnitudes quickly exceed the small disturbance assumptions made, and that more complex models must be used to accurately characterize the open-loop response. However, with the LQR controller implemented the model stays within the bounds of the original assumptions and the results are deemed acceptable. The tailless R-UAV can be stabilized using LQR in all three flight conditions.

It should be emphasized here again that the active control studies presented here at not meant to be comprehensive and definitive. These are exploratory studies aimed at evaluating whether the configuration can be stabilized using its control surfaces and what the order of magnitude of required control activity would be.

Chapter 9
CONCLUSION

9.1 Final Results

The preceding chapters have shown that using canards in symmetric and differential motion together with wing trailing-edge flaps, ailerons, and drag devices, a supersonic long-range configuration can be stabilized and controlled at low-speeds without a vertical tail using active control at both low and high angles of attack. The most severe cases, needing yaw authority, are an engine-out take-off and low-speed flight. It was shown that, for the 2014 UW R-UAV, the lateral-directional stability was heavily dependent on the dynamic pressure, and therefore directly related to the speed of the aircraft.

This is not surprising, given earlier research programs such as the Innovative Control Effectors (ICE) [23] , [24] which showed that stability and handling qualities at low subsonic conditions are expected to be the critical situations for supersonic aircraft given the reduced aerodynamic effectiveness at low dynamic pressure. The 2014 UW R-UAV and the S&C research it makes possible are, thus, very valuable in light of such findings.

Moreover, regarding the small scale of the 2014 UW R-UAV and differences in Reynolds numbers between R-UAV scale and full scale - Reynolds number scale effects on the thin highly swept type planforms have a small effect on S&C because of the leading edge controlled separation and resulting vortex action, which are not viscous dominated flows. This was reported in published data, as well as confirmed by CFD runs at various Reynolds numbers and wind tunnel testing of the configuration at the University of Washingtons Kirsten Wind Tunnel (KWT) over a range of airspeeds. As

to Mach number effects - The Mach effects up to 0.8 can also be small for slender thin-wing aircraft. The R-UAV and KWT results should be useful regarding application to a full-scale aircraft up to Mach 0.8 subsonic flight.

While low observability (stealth) was outside the scope of the 2014 University of Washington capstone airplane design project and this thesis, it is worthwhile to note that qualitatively the 2014 UW R-UAV configuration without the vertical tail and with only the small dihedraled canards has the potential to result in observability as low as that of the YF-23's V-tail arrangement or better in military applications.

A few additional findings of importance that require attention: A sensitivity of dynamic behavior to the Ixz product of inertia; the effect of canard / wing aerodynamic interaction and canard / vertical tail aerodynamic interactions due to canard-generated vortex systems; the importance of front-fuselage cross-section shaping using chines; the differences between the R-UAV with conventional and low-boom forward fuselage.

To summarize: The 2014 UW R-UAV can provide important and useful stability and control information, based on analysis, wind tunnel, and flight tests, that would benefit designers of long-range supersonic configurations. This thesis describes a comprehensive effort to develop linearized state space models for this configuration and it reports exploratory results regarding the feasible control of such a configuration without a vertical tail. The thesis also includes a rich bibliography covering all aspects of the tailless configuration stability and control problem including, in addition to the references mentioned so far, also Refs [25]-[32].

9.2 Future Work

There are many possibilities and needs for continued research based on the work presented here. The work of this thesis can be extended directly, and, in addition, a few interesting avenues have been identified that should be explored. The most pressing and promising items that should be considered for future research are listed

below:

- Flight testing that would generate usable results from the data acquisition system. Flight testing would give the ability to infer "real world" rotary derivatives and validate static stability parameters in "free air", without the wind tunnel support interference and wall effects. This should include servo positions and what that means for the control surface deflection, as well as pilot inputs to the system separated from the inputs produced from the gyros. Flight test results should be compared to simulation results and the simulation models should be modified accordingly, taking into account the uncertainties involved in flight tests.

- Designing controllers that are more advanced than the exploratory controller studied here, actually implementing them on the R-UAV, and flying with smaller tails. This includes looking into using the differential canard as part of the primary yaw control system. This set up would give significantly more yaw control and could perhaps eliminate the need for a tail at the extreme yaw control demand of an engine out on take-off.

- Taking a careful look at how the Ixz moment of inertia will change with the removal of the vertical tail. It has been shown that the dutch roll stability of the configuration is very sensitive to this parameter. The vertical tail area is one of the main contributors to this Ixz term and special care may need to be taken to re-balance the aircraft with weights to restore the Ixz term to a value that will still give acceptable dutch roll characteristics for the aircraft. Also investigate canard vortex interference of vertical tail and wings as a contributor to low dutch roll stability.

- Analysis and flight tests of the R-UAV in its low-boom long-nose design using the already acquired wind tunnel data, including multiple nose cross-sections.

- A Multidisciplinary Design Optimization (MDO) study to examine the net weight and complexity of drag rudder type systems compared to designs with a vertical tail and rudder.

- Additional forebody cross-sectional shapes can be studied in a subsequent wind tunnel entry of the model. Such shapes can potentially eliminate some yaw slice.

The list above focuses on problems that can be studied using the 2014 UW R-UAV essentially as-is (with just minor modification for a long front fuselage, if pursued), without having to make large investments into any major design modifications or new models.

BIBLIOGRAPHY

[1] Livne, E. and Nelson, C., "From Blank Slate to Flight Ready New Small Research UAVs in Twenty Weeks - Undergraduate Airplane Design at the University of Washington," AIAA Paper 2012-0845, AIAA Aerospace Sciences Meeting, Nashville, TN, January 9 - 12 2012.

[2] Colgren, R. and Loschke, R., "To Tail or Two Tails? - The Effective Design and Modeling of Yaw Control Devices," AIAA Paper 2002-4609, AIAA, 2002.

[3] University of Washington, "2014 Aircraft Design: Project STORM," Final Report and Presentation.

[4] Reithmaier, L., *Mach 1 and Beyond*, McGraw-Hill, 1995.

[5] Conway, E. M., *High-Speed Dreams. NASA and the Technopolitics of Supersonic Transportation 1945-1999*, New Series in NASA History, The Johns Hopkins University Press, 2005.

[6] Nelson, C., "Effects of wing planform on HSCT off-design aerodynamics," *10th Applied Aerodynamics Conference*, Jun 1992.

[7] Bhatia, K. and Werthmeimer, J., "Aeroelastic Challenges For A High Speed Civil Transport," *34th Structures, Structural Dynamics and Materials Conference*, Apr 1993.

[8] Solies, U., "Low speed handling qualities of the High Speed Civil Transport," *Aircraft Engineering, Technology, and Operations Congress*, Sep 1995.

[9] Mejia, K., "A comprehensive review of high speed wind tunnel performance data from the Boeing High Speed Civil Transport Program," *39th Aerospace Sciences Meeting and Exhibit*, Jan 2001.

[10] Kaminer, I. I., Howard, R. M., and Buttrill, C. S., "Development of Closed-Loop Tail-Sizing Criteria for a High Speed Civil Transport," *Journal of Aircraft*, Vol. 34, No. 5, Sep 1997, pp. 658664.

[11] Schutte, J. and Mavris, D. N., "Evaluation of N+2 Technologies and Advanced Vehicle Concepts," *53rd AIAA Aerospace Sciences Meeting*, Jan 2015.

[12] Magee, T., Fugal, S., Fink, L., and Shaw, S., "Boeing N+2 Supersonic Experimental Validation Phase II Program," *32nd AIAA Applied Aerodynamics Conference*, Jun 2014.

[13] Morgenstern, J., Buonanno, M., and Norstrud, N., "N+2 Low Boom Wind Tunnel Model Design and Validation," *30th AIAA Applied Aerodynamics Conference*, Jun 2012.

[14] Buonanno, M., Chai, S., Marconi, F., and Morgenstern, J. M., "Overview of Sonic Boom Reduction Efforts on the Lockheed Martin N+2 Supersonic Validations Program," *32nd AIAA Applied Aerodynamics Conference*, Jun 2014.

[15] Garzon, A. and Matisheck, J., "Supersonic Testing of Natural Laminar Flow on Sharp Leading Edge Airfoils. Recent Experiments by Aerion Corporation," *42nd AIAA Fluid Dynamics Conference and Exhibit*, Jun 2012.

[16] Schmidt, L. V., *Introduction to Aircraft Flight Dynamics (AIAA Education Series)*, American Institute of Aeronautics and Astronautics, 1998.

[17] Giesing, J. P. and Rodden, W. P., "Application of oscillatory aerodynamic theory to estimation of dynamic stability derivatives," *Journal of Aircraft*, Vol. 7, No. 3, May 1970, pp. 272–275.

[18] Rodden, W. P., Bellinger, E. D., and Giesin, J. P., "Errata and Addenda to Application of Oscillatory Aerodynamic Theory to Estimation of Dynamic Stability Derivatives," *Journal of Aircraft*, Vol. 21, No. 1, Jan 1984, pp. 93–94.

[19] Chen, P.C., L. H. W. and Liu, D. D., "Unsteady Subsonic Aerodynamics for Bodies and Wings with External Stores Including Wake Effect," *Journal of Aircraft*, Vol. 30, No. 5, 1993, pp. 618–628.

[20] Chen, P. C. and Liu, D. D., "Unsteady Supersonic Computations of Arbitrary Wing-Body Configuration Including External Stores," *Journal of Airc*, Vol. 27, No. 2, 1990, pp. 108–116.

[21] Hespanha, J. P., "Lecture notes on LQR/LQG controller design," January 2005.

[22] Frank Lewis, D. V. and Syrmos, V., *Optimal Control*, John Wiley & Sons, Inc., 3rd ed., 2012.

[23] Roetman, E. L., N. S. and Dawdy, J. R., "Innovative Control Effectors (ICE)," Tech. rep., DTIC, 1996.

[24] Dorsett, K. and Mehl, D., "Innovative Control Effectors (ICE)," Tech. rep., DTIC Document, 1996.

[25] A.J. Calis, S. L. and Sharma, M., "Development of a Reconfigurable Flight Control Law for Tailless Aircraft," *Journal of Guidance, Control, and Dynamics*, Vol. 24, 2001, pp. 896–902.

[26] Brinker, J. . and Wise, K., "Flight Testing of Reconfigurable Control Law on the X-36 Tailless Aircraft," *Journal of Guidance, Control, and Dynamics*, Vol. 24, 2001, pp. 903–909.

[27] Colgren, R. and Loschke, R., "Effective Design of Highly Maneuverable Tailless Aircraft," *Journal of Aircraft*, Vol. 45, 2008, pp. 1441–1449.

[28] Ericksson, L. and Beyers, M., "High-Alpha Aerodynamics of a Slender Tailless Aircraft Configuration," AIAA Paper 2002-0094, AIAA, 2002.

[29] Ringertz, U. and Stenfelt, G., "Yaw Departure and Recovery of a Tailless Aircraft," *Journal of Aircraft*, Vol. 50, No. 1, 2013, pp. 311–314.

[30] Stenfelt, G. and Ringertz, U., "Yaw Control of a Tailless Aircraft Configuration," *Journal of Aircraft*, Vol. 47, No. 5, 2010, pp. 1807–1810.

[31] Stenfelt, G. and Ringertz, U., "Lateral Stability and Control of a Tailless Aircraft Configuration," *Journal of Aircraft*, Vol. 46, 2009, pp. 2161–2164.

[32] Wells, S. and Hess, R., "Multi-Input/Multi-Output Sliding Mode Control for a Tailless Fighter Aircraft," *Journal of Guidance, Control, and Dynamics*, Vol. 26, 2003, pp. 463–473.

Appendix A

WIND TUNNEL COORDINATE SYSTEMS

All stability coefficients and derivatives were taking from the UWAL stability axes. The diagram is below in Figure A.1. Additional information, including this diagram can be found on the UWAL website (www.uwal.org).

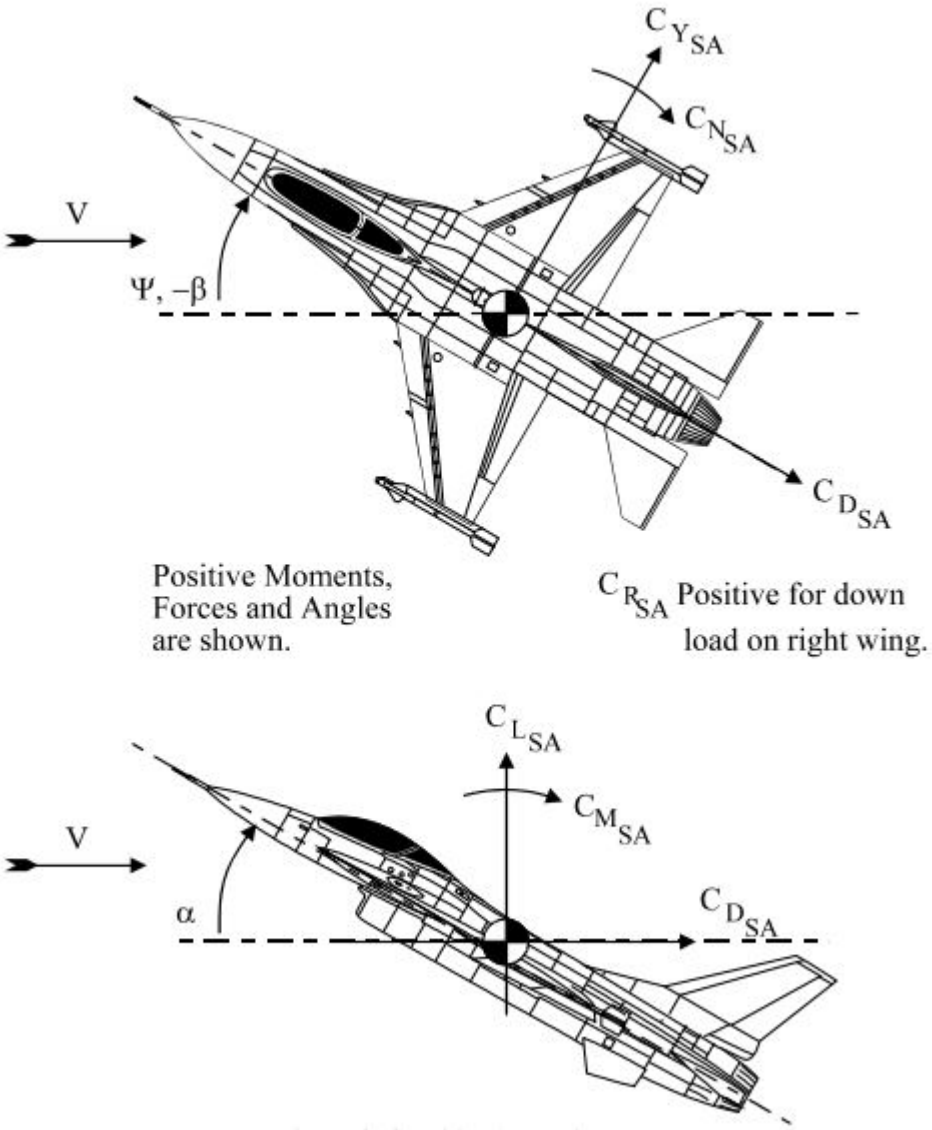

Figure A.1: Stability Axes Diagram